J. Fluid Mech. (2013), *vol.* 714, *pp.* 95–126. © Cambridge University Press 2013
doi:10.1017/jfm.2012.461

The sharp-interface limit of the Cahn–Hilliard/Navier–Stokes model for binary fluids

F. Magaletti[1], F. Picano[1,2], M. Chinappi[3], L. Marino[1] and C. M. Casciola[1]†

[1] Dipartimento di Ingegneria Meccanica e Aerospaziale, Università di Roma La Sapienza, Via Eudossiana 18, 00184 Roma, Italy

[2] Linné Flow Center, KTH Mechanics, Osquars Backe 18, SE-100 44 Stockholm, Sweden

[3] Dipartimento di Fisica, Università di Roma La Sapienza, P. le Aldo Moro 5, 00185 Roma, Italy

(Received 2 April 2012; revised 3 August 2012; accepted 14 September 2012)

The Cahn–Hilliard model is increasingly often being used in combination with the incompressible Navier–Stokes equation to describe unsteady binary fluids in a variety of applications ranging from turbulent two-phase flows to microfluidics. The thickness of the interface between the two bulk fluids and the mobility are the main parameters of the model. For real fluids they are usually too small to be directly used in numerical simulations. Several authors proposed criteria for the proper choice of interface thickness and mobility in order to reach the so-called 'sharp-interface limit'. In this paper the problem is approached by a formal asymptotic expansion of the governing equations. It is shown that the mobility is an effective parameter to be chosen proportional to the square of the interface thickness. The theoretical results are confirmed by numerical simulations for two prototypal flows, namely capillary waves riding the interface and droplets coalescence. The numerical analysis of two different physical problems confirms the theoretical findings and establishes an optimal relationship between the effective parameters of the model.

Key words: capillary flows, drops and bubbles, diffuse interface methods, interfacial flows (free surface)

1. Introduction

Binary flows appear in several natural phenomena and in a large number of engineering applications ranging from spray and aerosol formation in turbulent flows (Marmottant & Villermaux 2004) to droplet and bubble transport in microfluidic devices (Thorsen *et al.* 2001). In all of these problems surface tension acts on a very thin layer between the two bulk fluids (typically three or four times the characteristic size of the fluid molecules) and plays a crucial role on macroscopic dynamics.

Two classes of approaches are used to describe binary flows: sharp- and diffuse-interface models. In the former, the narrow zone separating the two immiscible fluids is described as a discontinuity in the fluids properties. The classical Navier–Stokes equations govern the hydrodynamic behaviour on both sides of the interface and jump conditions on stresses and velocities are prescribed across the interface.

† Email address for correspondence: carlomassimo.casciola@gmail.com

https://doi.org/10.1017/jfm.2012.461 Published online by Cambridge University Press

A straightforward way of handling the moving interface is employing a mesh on the discontinuity surface which deforms according to the flow. Front tracking (Unverdi & Tryggvason 1992; Tryggvason *et al.* 2001) and volume of fluid methods (Hirt & Nichols 1981; Menard, Tanguy & Berlemont 2007) are examples of this approach. Accurate results can be obtained following this philosophy, but substantial difficulties arise in high curvature regions and *ad hoc* smoothing rules are needed to guarantee numerical convergence of the method (Sussman & Puckett 2000; Renardy & Renardy 2002).

As an alternative, the interface between two immiscible fluids can be described as a thin layer where fluid properties change smoothly. The basic idea can be traced back to Van der Waals in 1894 (translated by Rowlinson in Van der Waals (1979)) who suggested to stabilize the interface formed in the binary mixture by weakly non-local (gradient) terms in the free energy. Cahn & Hilliard (1958) used this approach in the context of a purely diffusional problem providing an evolution equation for the concentration field. The thermodynamic consistency of the coupled Cahn–Hilliard/Navier–Stokes model (Gurtin, Polignone & Vinals 1995; Qian, Wang & Sheng 2006; Ren *et al.* 2011) and its ability to handle topological changes are the principal reasons that justify the increasingly common adoption of diffuse-interface methods (Jacqmin 2000; Badalassi, Ceniceros & Banerjee 2003; Yue *et al.* 2005; Ding, Gilani & Spelt 2010; Carlson, Bellani & Amberg 2012).

The fundamental variable of the Cahn–Hilliard model is the scalar phase field $\Phi(\boldsymbol{x}, t)$ which describes the relative quantity of one of the two phases of the binary system, with $\boldsymbol{x}$ and t position and time, respectively, and with the two pure fluids corresponding to $\Phi = 1$, $\Phi = -1$. The two fluids are immiscible, implying that the flow domain is essentially partitioned into disjoined subdomains, each occupied by a single pure fluid, separated by an extremely narrow interface where $-1 < \Phi < 1$ and the two substances partially mix. In fact, in ordinary conditions, the physical thickness of the interface is on the nanometre scale and the model can be numerically exploited for microscale and macroscale applications only at the price of an artificial thickening of the interface.

In addition to the interface thickness ℓ, another parameter appears in the model: the mobility M. While the value of ℓ is a well-defined quantity which can be measured and is typically of the order $\ell \simeq 10^{-9}$ m, the proper value of the mobility M is more difficult to establish. This parameter resembles the local mass diffusivity between the two fluids which takes place at the interface level on a molecular scale. Assuming that the diffusive length scale is comparable with molecular dimensions, Jacqmin (2000) proposed an order of magnitude estimate of $\sim 10^{-17}$ m^3 s kg^{-1} for the mobility. It is clear that affordable values for interface thickness and mobility need to be much larger than suggested by physical considerations in order to make simulations affordable. On the other hand, if empirically tuned parameters are adopted, the results need to be compared with analytical or experimental results available beforehand. Before closing these introductory comments, it is also worthwhile mentioning that even the physical (i.e. at least conceptually amenable of direct measurement) definition of mobility is not entirely obvious.

In this ambiguous context is crucially important to assess existence and properties of the 'sharp-interface limit' of the model, an asymptotic state where the interface dynamics becomes macroscopically independent of the specific values of ℓ and M or, equivalently, of the Cahn (Cn) and the mobility number (M^*) to be introduced below. In this limit, the thin interface will be convected by the local fluid velocity, with at most asymptotically small corrections; meanwhile, a capillary stress will act on the

https://doi.org/10.1017/jfm.2012.461 Published online by Cambridge University Press

thin, diffused interfacial layer coherently with the classical Young–Laplace law where the interface-borne stress is proportional to surface tension and interface curvature and is directed along the interface normal. Introducing a consistent and practically useful theory of how these objectives can be achieved by suitable, intrinsically related choices of the parameters Cn and M^* is the main purpose of the present paper.

The issue has already been pursed by other researchers with results which are still not entirely conclusive. With no claim of completeness, to the author's knowledge, one of the most exhaustive papers on the subject is that of Lowengrub & Truskinovsky (1998). By dealing with the quasi-incompressible Euler/Cahn–Hilliard model, it was shown through asymptotic expansions that the ratio M^*/Cn must be extremely small $M^*/Cn \ll 1$, suggesting as viable solutions $M^* \propto Cn$ and $M^* \propto Cn^2$ for vanishingly small Cahn number. The results, although interesting, are limited to inviscid flows and do not succeed in establishing a clear-cut scaling law between the two parameters. Successively Jacqmin (1999) dealt with the problem and stated that the mobility has to decrease with a power of the interface thickness, i.e. in our dimensionless form $M^* \propto Cn^\alpha$, with $1 \leqslant \alpha < 2$, based on order of magnitude arguments concerning diffusion, strain and chemical potential. More recently, other authors (Khatavkar, Anderson & Meijer 2006) approached the problem on numerical grounds, proposing the scaling $M^* \propto 1/Cn$ without providing a complete theoretical framework and reporting difficulties associated with topological transitions. Huang, Shu & Chew (2009) focused on the mobility showing by numerical results a mobility-dependent bifurcation in the dynamics of capillarity-driven flows. Finally, Yue, Zhou & Feng (2010) have investigated the requirements for a simulation including a moving contact line, using both numerical experiments and scaling arguments, and propose to keep the mobility constant in approaching the limit of vanishing interface thickness. As we see the debate is still open and there is space for discussing a general strategy to approach the sharp-interface limit based on a new theory in terms of a consistent matched asymptotic analysis.

The paper is structured as follows: the asymptotics is presented in § 2 where the complete solution is obtained by proper matching of inner and outer solutions. The inner expansion involves the small parameter Cn^3/M^* while the external field is expanded in M^*/Cn. The use of two *a priori* different expansion parameters follows by precise dynamic constraints. On the one hand, recovering the correct surface stress is mandatory. On the other hand, the interface has to be advected by the external velocity field. Matching the two expansions in the overlap layers above and below the nominal interface determines the full solution and allows both expansion parameters to be identified with the Cahn number, thereby providing the sharp prediction $M^* \propto Cn^2$ for the mobility in terms of interface thickness.

In addition to two expected length scales, two different time scales emerge quite naturally. The main line of the theoretical procedure is provided in § 2.2 mainly focusing on the outer, slow time scale and presenting the basic results. Successively, the dissipative mechanisms which drive the system toward equilibrium are discussed in § 2.3 to analyse the fast time scale dynamics in detail.

The results of the theory have been applied to two prototypal problems, namely capillary wave propagation on the interface between the immiscible fluids, § 3.2, and coalescence of two droplets, § 3.3. The evolution of capillary waves is a well-understood and classical problem of the fluid mechanics (Chandrasekhar 1961; Prosperetti 1981; Jeng *et al.* 1998) and represents a benchmark to test numerical algorithms and mathematical models (Jacqmin 1999; Kim 2005) in the simplest geometry where the interface drives the flow. The coalescence of two droplets is

https://doi.org/10.1017/jfm.2012.461 Published online by Cambridge University Press

an even more fundamental interface-driven problem which is still free of additional difficulties associated with fluid–wall interactions. In particular, the topological transition which occurs during the coalescence is a nice example of the rich physics involved in interfacial phenomena.

2. Asymptotics of the Cahn–Hilliard/Navier–Stokes model for the interface

2.1. *Theoretical background*

The molecular modelling of the interface dates back to Van der Waals in 1894 (translated by Rowlinson in Van der Waals 1979). More recently, in seminal papers (Fisk & Widom 1969; Triezenberg & Zwanzig 1972) (the 1972 paper should be considered as 'first', since from the authors comment it communicates with a more concise original derivation an unpublished 1948 result of Yvonne's) statistical mechanics is used to provide the link between surface tension σ and equilibrium particle number density profile $n_0(z)$ of a planar liquid–vapour interface with normal in the z direction,

$$\sigma = \frac{1}{6} k_B T \ell_z^2 \int_{-\infty}^{\infty} \left(\frac{\mathrm{d}n_0}{\mathrm{d}z} \right)^2 \mathrm{d}z, \tag{2.1}$$

where k_B is the Boltzmann constant, T the temperature and ℓ_z a characteristic length. The mass density profile of the fluid follows as $\rho(z) = m n_0(z)$, with m being the molecular mass. This expression associates the surface tension to the transition layer between the two different phases and implicitly calls the attention to a diffuse-interface description of capillary phenomena.

In fact, everyday experience suggests that the interface between two immiscible fluids is optically sharp. In other words the layer separating the two bulk phases is too thin to be detected by light in the visible range of wavelengths. More accurate checking of the interface, e.g. by neutron or X-ray scattering experiments on a prototype interface between water and *n*-alkyl (Mitrinović *et al.* 2000), actually shows that the transition layer is in the nanometre range as consistently found also by molecular dynamics simulations, see e.g. Giacomello *et al.* (2012).

The molecular nature of the interface has been exploited in a number of molecular dynamics (MD) simulations which essentially confirm the extremely small thickness of the interface (few times the molecular size for temperature sufficiently below the critical; Nijmeijer *et al.* 1988). In general terms the problem of reconciling the hydrodynamic description of the interface with its molecular origin is still open, see the recent proposal in Orlandini, Meloni & Ciccotti (2011).

Continuum models for the interface in the spirit of the Cahn–Hilliard model (Cahn & Hilliard 1958, 1959) are phenomenologically introduced in terms of a suitable non-local free energy functional $F[\Phi]$ where the scalar $\Phi(\boldsymbol{x}, t)$, function of position and time, is called the phase field. It can be defined as $\Phi = (n_2 - n_1)/(n_2 + n_1)$ with n_1 and n_2 the particle number densities of the two species in the case of a binary system, or of the two phases in the case of a single-component fluid. In this framework the structure of the functional reproduces the main features of the statistical mechanics description, providing an expression for the surface tension analogous to (2.1). The free energy functional reads

$$F[\Phi] = \int_{\Omega} \frac{3}{2\sqrt{2}} \sigma \ell \left[f_{bulk}(\Phi) + \frac{1}{2} |\nabla \Phi|^2 \right] \mathrm{d}V + \int_{\partial\Omega} f_w(\Phi) \, \mathrm{d}S \tag{2.2}$$

https://doi.org/10.1017/jfm.2012.461 Published online by Cambridge University Press

where the boundary term with wall potential f_w extends the model to fluid–wall interactions, see e.g. Jacqmin (2000). In (2.2) Ω is the flow domain, the parameter σ will be shown to be the surface tension, ℓ is the typical interface thickness, with the numerical factor included for convenience. The equilibrium profile for the phase field corresponds to a minimum of the free energy and determines the position of the interface. The double well shape of the bulk free energy density, $f_{bulk} = (\Phi^2 - 1)^2/(4\ell^2)$, with two minima $\Phi = \pm 1$ in the two pure fluids, drives the system towards the segregation of the two phases. The process of segregation is restrained by the second term $1/2\,|\nabla\Phi|^2$ which energetically penalizes the formation of the interface. It accounts for the interfacial energy which originates at the molecular level and allows for a limited miscibility between the two species. A consequence of these two opposite driving forces is a finite thickness interface (width order ℓ), across which the phase field changes smoothly between its extremal values. Based on experimental evidence, the interface thickness is extremely thin when compared with the outer scales of the system (e.g. the characteristic dimension of the flow domain), implying that the Cahn number, the ratio of the two, is vanishingly small.

The model can be extended to unsteady conditions by assuming that a phase current $\boldsymbol{J}[\Phi]$ tends to drive the system towards equilibrium according to the kinetic equation $\mathrm{D}\Phi/\mathrm{D}t = -\nabla\cdot\boldsymbol{J}$ (Cahn & Hilliard 1958, 1959). The current $\boldsymbol{J} = -M\nabla\mu_c$ is taken proportional to the gradient of the chemical potential μ_c, defined as the functional derivative of the free energy $\mu_c = \delta F/\delta\Phi = 3\sigma(\Phi^3 - \Phi - \ell^2\nabla^2\Phi)/(2\sqrt{2}\ell)$. Usually, for the sake of simplicity, the proportionality factor between current and chemical potential gradient, the mobility M, is assumed constant. The Cahn–Hilliard equation then follows:

$$\frac{\partial\Phi}{\partial t} + \boldsymbol{u}\cdot\nabla\Phi = \frac{3M\sigma}{2\sqrt{2}\ell}\nabla^2(\Phi^3 - \Phi - \ell^2\nabla^2\Phi). \tag{2.3}$$

For the problems we are interested in, the evolution of the phase field is associated with a significant fluid motion. The velocity field $\boldsymbol{u}$ is described by the incompressible Navier–Stokes equations coupled to the phase field by the surface tension term proportional to $\nabla\Phi$ (see, e.g., Jacqmin 2000; Yue *et al.* 2010), leading to the complete system

$$\nabla\cdot\boldsymbol{u} = 0, \tag{2.4a}$$

$$\frac{\partial\boldsymbol{u}}{\partial t} + \boldsymbol{u}\cdot\nabla\boldsymbol{u} = -\nabla p + \frac{1}{Re}\nabla^2\boldsymbol{u} + \frac{3}{2\sqrt{2}}\frac{1}{We\,Cn}(\Phi^3 - \Phi - Cn^2\nabla^2\Phi)\nabla\Phi, \tag{2.4b}$$

$$\frac{\partial\Phi}{\partial t} + \boldsymbol{u}\cdot\nabla\Phi = \frac{M^*}{Cn}\nabla^2[\Phi^3 - \Phi - Cn^2\nabla^2\Phi]. \tag{2.4c}$$

The equations are written in dimensionless form, with position $\boldsymbol{x}$ normalized by an outer length scale λ and the velocity by $\omega\lambda$, where ω is a characteristic frequency. $M^* = 3M\sigma/(2\sqrt{2}\lambda^3\omega)$ is a dimensionless number representing the mobility (the mobility number or mobility parameter), $Re = \rho\lambda^2\omega/\mu$ the Reynolds number, $We = \rho\omega^2\lambda^3/\sigma$ the Weber number and $Cn = \ell/\lambda$ the Cahn number. The ratio Cn/M^* is often interpreted as the effective Péclet number of the system.

To the best of the present authors' knowledge, the mobility is hardly amenable of direct experimental measurement for a molecularly sharp interface. Hence, it is interpreted here as an effective parameter of the model, to be selected in view of reaching the sharp-interface limit of the equations. We emphasize that the mobility M introduces an intrinsic time scale associated with the relaxation towards the

https://doi.org/10.1017/jfm.2012.461 Published online by Cambridge University Press

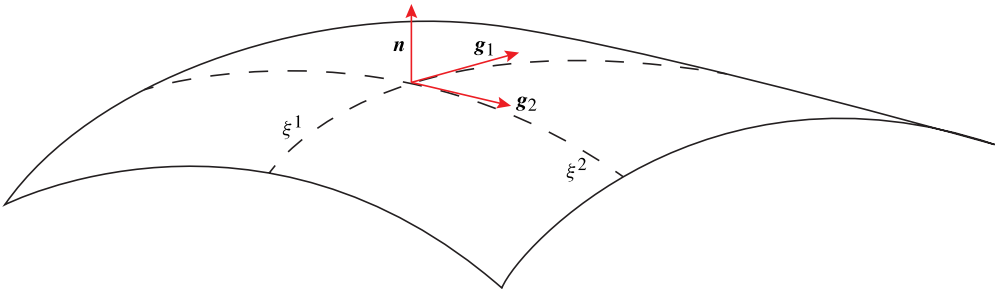


FIGURE 1. (Colour online) Sketch of the curved interface with the local coordinates $\boldsymbol{\xi} = (\xi^1, \xi^2)$ and local tangent $\boldsymbol{g}_\alpha$ (covariant base) and normal $\boldsymbol{n}$ vectors.

equilibrium profile. The process is contrasted by the flow advection occurring on the outer time scale. The ratio of the two, related to the mobility number M^*, has a major impact on the dynamics of the system. The purpose of this paper is to understand how the dimensionless interface thickness Cn and mobility parameter M^* should be related in order to asymptotically guide the solution of the diffuse-interface model towards the sharp interface behaviour observed in the experiments in the limit of vanishing interface thickness. The physical interpretation is that the mobility should suitably change as the interface thickness keeps on reducing, in order to maintain the effective interface force consistent with the required surface tension (2.1).

2.2. *Matched asymptotic expansions and the sharp-interface limit*

An inner/outer expansion of the relevant fields is used to describe the evolution of the interfacial layer and of the two pure fluids above and below the interface, respectively. Recovering the correct physical behaviour of the interface by matching the three solutions identifies the proper distinguished limit (Kevorkian & Cole 1996).

Since the interface is unsteady, a coordinate frame attached to the moving interface is appropriate (see figure 1). The interface is defined by the implicit equation $\Phi(\boldsymbol{x}, t) = 0$, i.e. its nominal position is taken to coincide with the zero isosurface of the phase field. Introducing the parametrization $\boldsymbol{\xi} = (\xi^1, \xi^2)$, an interface point is given as $\boldsymbol{x} = \boldsymbol{x}_I(\boldsymbol{\xi}, t)$, with $\Phi[\boldsymbol{x}_I(\boldsymbol{\xi}, t), t] \equiv 0$. It follows

$$\frac{\mathrm{D}\Phi[\boldsymbol{x}_I(\boldsymbol{\xi}, t), t]}{\mathrm{D}t} = \frac{\partial \Phi}{\partial t} + \dot{\boldsymbol{x}}_I \cdot \boldsymbol{\nabla}\Phi = \frac{\delta \Phi}{\delta t} + \boldsymbol{v} \cdot \nabla_\pi \Phi, \tag{2.5}$$

where $\boldsymbol{v} = \dot{\boldsymbol{x}}_I$, $\boldsymbol{\nabla}_\pi$ is the component of the gradient tangent to the interface and $\delta\Phi/\delta t = \partial\Phi/\partial t + v_n \partial\Phi/\partial\zeta$ ($\partial/\partial\zeta = \boldsymbol{n} \cdot \boldsymbol{\nabla}$) is the displacement derivative (Truesdell & Toupin 1960) introduced to avoid using objects such as $\partial\Phi/\partial t$ and $\partial\Phi/\partial\zeta$ which become ill behaved across the interface, once the sharp-interface limit is taken. The standard covariant base vectors $\boldsymbol{g}_\alpha = \partial\boldsymbol{x}/\partial\xi^\alpha$ and normal $\boldsymbol{n} = (\boldsymbol{g}_1 \times \boldsymbol{g}_2)/|\boldsymbol{g}_1 \times \boldsymbol{g}_2|$ on the interface allow to write the differentiation operators as

$$\boldsymbol{\nabla} = \boldsymbol{n}\frac{\partial}{\partial\zeta} + \boldsymbol{g}^\alpha \frac{\partial}{\partial\xi^\alpha} \tag{2.6a}$$

$$\nabla^2 = \frac{\partial^2}{\partial\zeta^2} + C^\alpha_{\ \alpha}\frac{\partial}{\partial\zeta} + \left(\boldsymbol{n} \cdot \frac{\partial \boldsymbol{g}^\beta}{\partial\zeta} - \Gamma^\beta_{\alpha\delta} g^{\alpha\delta}\right)\frac{\partial}{\partial\xi^\beta} + g^{\alpha\beta}\frac{\partial^2}{\partial\xi^\alpha \partial\xi^\beta}, \tag{2.6b}$$

https://doi.org/10.1017/jfm.2012.461 Published online by Cambridge University Press

where ζ is the coordinate along the interface normal, $C_\alpha^\alpha = \nabla_\pi \cdot \boldsymbol{n}$ is the interface curvature, $\Gamma_{\alpha\beta}^\delta = \boldsymbol{g}^\delta \cdot \partial \boldsymbol{g}_\alpha / \partial \xi^\beta$ the Cristhoffel's symbols, and $\boldsymbol{g}^\alpha$ the contravariant tangent vectors ($\boldsymbol{g}^\alpha \cdot \boldsymbol{g}_\beta = \delta_\beta^\alpha$) (Aris 1989). The equation of the interface is simply $\zeta = 0$ in local coordinates.

In system (2.4) the Cahn number (dimensionless width of the diffuse interface) is certainly a small geometrical parameter. Given a generic field $f(\boldsymbol{x}, t)$, in the limit of small Cn, the inner expansion should involve the rescaled normal distance $\eta = \zeta / Cn$ in order to keep staying inside the transition layer at reducing Cahn number. After expressing the position in terms of the local coordinates $\boldsymbol{\xi}, \eta$, the inner expansion is

$$f^{(i)}(\boldsymbol{\xi}, \eta, t) = \lim_{\substack{Cn \to 0 \\ \eta = \zeta / Cn = \text{cost}}} f(\boldsymbol{\xi}, \zeta / Cn, t). \tag{2.7}$$

Similarly, the outer expansion is obtained in the limit of vanishing interface thickness, keeping the distance to the interface constant with respect to the outer length scale λ, i.e. $\zeta = \text{const}$,

$$f^{(e)}(\boldsymbol{\xi}, \zeta, t) = \lim_{\substack{Cn \to 0 \\ \zeta = \text{cost}}} f(\boldsymbol{\xi}, \zeta, t). \tag{2.8}$$

Inner and outer expansions need to be matched in the two overlap layers above and below the nominal interface,

$$\lim_{\zeta \to 0^+} f^{(e)}(\boldsymbol{\xi}, \zeta, t) = \lim_{\eta \to +\infty} f^{(i)}(\boldsymbol{\xi}, \eta, t), \quad \lim_{\zeta \to 0^-} f^{(e)}(\boldsymbol{\xi}, \zeta, t) = \lim_{\eta \to -\infty} f^{(i)}(\boldsymbol{\xi}, \eta, t). \tag{2.9}$$

The matching conditions then allow us to express the jump $[[f^{(e)}]]$ of the outer variable across the interface in terms of the inner solution $f^{(i)}$,

$$[[f^{(e)}(\boldsymbol{\xi}, t)]] = \lim_{\zeta \to 0^+} f^{(e)}(\boldsymbol{\xi}, \zeta, t) - \lim_{\zeta \to 0^-} f^{(e)}(\boldsymbol{\xi}, \zeta, t) = \int_{-\infty}^{+\infty} \frac{\partial}{\partial \eta} f^{(i)}(\boldsymbol{\xi}, \eta, t) \, \mathrm{d}\eta. \tag{2.10}$$

In this general framework, the problem is identifying the correct expansion parameter for both inner and outer solution. As discussed in § 1 the issue is not entirely trivial, since the effect of the mobility parameter on the dynamics makes the matter a little more complicated than the straightforward identification of the expansion parameter with the Cahn number. At any rate, once the expansion parameter is selected, the standard asymptotic procedure will allow us to find the inner and outer solutions at different orders in the expansion to successively match them, order by order, in the two overlap layers expected to exist above and below the interface. We stress that it is actually the matching procedure the step which forces the expansion parameter to be the same for inner and outer fields. The parameter is not available beforehand, with the further difficulty that experiments cannot help in guiding towards the correct value of the mobility. We must be content to proceed on a heuristic basis, keeping the parameter undefined, until the matching procedure and the physical intuition will suggest the correct choice.

Let us start by addressing the outer expansion in detail. Looking at the equations, the Cahn number appears in the crucial term of (2.4*c*) in combination with the mobility parameter, M^*/Cn. The mobility is expected to be itself an extremely small quantity (Jacqmin 2000). With two small parameters at hand, several different scenarios are possible in principle. The correct recipe is characterized by its ability in reproducing the sharp-interface behaviour observed so cleanly in the experiments. The ansatz here is that M^*/Cn should vanish as the Cahn number is reduced. Evidence

https://doi.org/10.1017/jfm.2012.461 Published online by Cambridge University Press

will be provided below that this is indeed the correct request. However, this single restriction is insufficient to determine the correct limiting behaviour. An additional constraint will be found by analysing the asymptotics of the inner field in terms of a formally different expansion parameter. The additional constraint will unambiguously determine how the two small quantities need to scale one with the other to allow the solution of the perturbative expansion approaching the physically relevant sharp-interface limit through classical matching.

Assuming for the time being M^*/Cn as the proper small parameter, in the spirit of matched asymptotic expansions, the outer solution $\boldsymbol{u}^{(e)}$, $\Phi^{(e)}$ is expressed as

$$f^{(e)} = f_0^{(e)} + \frac{M^*}{Cn} f_1^{(e)} + O\left(\frac{M^*}{Cn}\right)^2. \tag{2.11}$$

Once inserted in system (2.4), this yields the leading order approximation for the two outer regions above and below the interface,

$$\boldsymbol{\nabla} \cdot \boldsymbol{u}_0^{(e)} = 0, \tag{2.12a}$$

$$\frac{\mathrm{D}\boldsymbol{u}_0^{(e)}}{\mathrm{D}t} = -\boldsymbol{\nabla} p_0^{(e)} + \frac{1}{Re}\nabla^2 \boldsymbol{u}_0^{(e)}, \tag{2.12b}$$

$$\frac{\mathrm{D}\Phi_0^{(e)}}{\mathrm{D}t} = 0. \tag{2.12c}$$

The standard Navier–Stokes equations combined with a pure advection equation for the phase field are recovered in the bulk phases from the complete system of (2.12), supporting the conjecture that the ansatz $M^*/Cn \to 0$ is reasonably correct.

The inner expansion of system (2.4) is treated with an analogous procedure. However, the natural expansion parameter for the inner field is still to be determined. Preliminarily the equation should be reorganized to arrange the different terms by order of magnitude, being aware that derivatives in the normal direction are extremely intense, order $1/Cn$ due to the thinness of the interface, while tangential derivatives are much smaller, order one. Denoting by $u_n^{(i)}$ and $\boldsymbol{u}_\pi^{(i)}$ the normal and tangent components of the fluid velocity, the system in inner variables reads

$$0 = \frac{1}{Cn}\frac{\partial u_n^{(i)}}{\partial \eta} + \boldsymbol{\nabla}_\pi \cdot \boldsymbol{u}_\pi^{(i)}, \tag{2.13a}$$

$$\begin{aligned}\frac{\delta u_n{}^{(i)}}{\delta t} + \left(u_n^{(i)} - v_n\right)\frac{1}{Cn}\frac{\partial u_n^{(i)}}{\partial \eta} + \left(\boldsymbol{u}_\pi^{(i)} - \boldsymbol{v}_\pi\right)\cdot\nabla_\pi u_n^{(i)} &= -\frac{1}{Cn}\frac{\partial p^{(i)}}{\partial \eta} \\ + \frac{1}{Re\,Cn^2}\left[\frac{\partial^2 u_n^{(i)}}{\partial \eta^2} + Cn\,C_\alpha^\alpha \frac{\partial u_n^{(i)}}{\partial \eta} + O(Cn^2)\right] \\ + \frac{3}{2\sqrt{2}}\frac{1}{We\,Cn^2}\left[\Phi^{(i)3} - \Phi^{(i)} - \frac{\partial^2 \Phi^{(i)}}{\partial \eta^2} - Cn\,C_\alpha^\alpha \frac{\partial \Phi^{(i)}}{\partial \eta} + O(Cn^2)\right]\frac{\partial \Phi^{(i)}}{\partial \eta},\end{aligned} \tag{2.13b}$$

$$\begin{aligned}\frac{\delta \boldsymbol{u}_\pi{}^{(i)}}{\delta t} + \left(u_n^{(i)} - v_n\right)\frac{1}{Cn}\frac{\partial \boldsymbol{u}_\pi^{(i)}}{\partial \eta} + \left(\boldsymbol{u}_\pi^{(i)} - \boldsymbol{v}_\pi\right)\cdot\nabla_\pi \boldsymbol{u}_\pi^{(i)} &= -\boldsymbol{\nabla}_\pi p^{(i)} \\ + \frac{1}{Re\,Cn^2}\left[\frac{\partial^2 \boldsymbol{u}_\pi^{(i)}}{\partial \eta^2} + O(Cn)\right],\end{aligned} \tag{2.13c}$$

https://doi.org/10.1017/jfm.2012.461 Published online by Cambridge University Press

$$\frac{\delta\Phi^{(i)}}{\delta t} + \left(u_n^{(i)} - v_n\right)\frac{1}{Cn}\frac{\partial\Phi^{(i)}}{\partial\eta} + \left(\boldsymbol{u}_\pi^{(i)} - \boldsymbol{v}_\pi\right)\cdot\nabla_\pi\Phi^{(i)}$$
$$= \frac{M^*}{Cn^3}\left\{\frac{\partial^2}{\partial\eta^2}\left[\Phi^{(i)3} - \Phi^{(i)} - \frac{\partial^2\Phi^{(i)}}{\partial\eta^2}\right]\right.$$
$$\left. + \; Cn\, C_\alpha^\alpha\frac{\partial}{\partial\eta}\left[\Phi^{(i)3} - \Phi^{(i)} - 2\frac{\partial^2\Phi^{(i)}}{\partial\eta^2}\right] + O(Cn^2)\right\}. \tag{2.13d}$$

After recalling that the displacement derivative has been introduced to ride the interface, the system for the inner solution is found to be characterized by the parameter M^*/Cn^3 in (2.13d). In principle, different asymptotic behaviours can be considered for M^*/Cn^3, provided that $M^* = o(Cn)$ as required to ensure consistency with the ansatz for the outer solution. For instance, both $M^* \propto Cn^2$ and $M^* \propto Cn^4$ satisfy this constraint. The two choices are, however, radically different since M^*/Cn^3 would approach infinity in the first case and zero in the other. We will shortly give a proof that the physics of a sharp interface between immiscible fluids calls for $Cn^3/M^* \to 0$ as $Cn \to 0$. Since the inner/outer expansion procedure should rely on a single parameter, by equating the two conjectured prescriptions yields

$$\frac{Cn^3}{M^*} = \frac{M^*}{Cn} \ll 1, \tag{2.14}$$

which is immediately reduced to

$$M^* \propto Cn^2 \ll 1, \tag{2.15}$$

allowing us to identify both expansion parameters with the Cahn number, $Cn^3/M^* = M^*/Cn = Cn \ll 1$. In this case the inner expansion reads

$$f^{(i)} = f_0^{(i)} + \frac{Cn^3}{M^*}f_1^{(i)} + O\left(\frac{Cn^3}{M^*}\right)^2. \tag{2.16}$$

Using this expansion in (2.13a), at leading order one obtains

$$\frac{\partial u_{n0}^{(i)}}{\partial\eta} = O(Cn). \tag{2.17}$$

The solution of this equation yields $u_{n0}^{(i)}(\eta) = \int_0^\eta O(Cn)\,\mathrm{d}\eta + u_{n0}^{(i)}(0)$ and, through (2.10), the leading order jump condition for the outer normal velocity component,

$$[[u_{n0}^{(e)}]] = 0. \tag{2.18}$$

With the proposed ansatz the normal velocity turns out to be continuous across the interface, as it should. The external velocity at the interface determines the interface displacement velocity

$$v_n = u_{n0}^{(e)}[\boldsymbol{x}_I(\boldsymbol{\xi}, t)] = u_{n0}^{(i)}(0). \tag{2.19}$$

By recalling the equations for the outer fields (2.12), it is now clear that the nominal interface is impermeable to the external flow, i.e. the material derivatives on the left-hand sides of (2.12) naturally follow the interface motion. As another consequence of (2.17) and (2.19) is that it follows $u_{n0}^{(i)} - v_n = O(Cn)$, implying that the leading order

https://doi.org/10.1017/jfm.2012.461 Published online by Cambridge University Press

terms in system (2.13) read

$$0 = -\frac{\partial p_0^{(i)}}{\partial \eta} + \frac{1}{Re}\frac{\partial}{\partial \eta}\left(\frac{1}{Cn}\frac{\partial u_{n0}^{(i)}}{\partial \eta}\right) - \frac{3}{2\sqrt{2}}\frac{C_\alpha^\alpha}{We}\left(\frac{\partial \Phi_0^{(i)}}{\partial \eta}\right)^2 + \frac{3}{2\sqrt{2}}\frac{1}{We\,Cn}\left(\Phi_0^{(i)3} - \Phi_0^{(i)} - \frac{\partial^2 \Phi_0^{(i)}}{\partial \eta^2}\right)\frac{\partial \Phi_0^{(i)}}{\partial \eta} + \frac{3}{2\sqrt{2}}\frac{1}{We}\left[\left(\Phi_0^{(i)3} - \Phi_0^{(i)} - \frac{\partial^2 \Phi_0^{(i)}}{\partial \eta^2}\right)\frac{\partial \Phi_1^{(i)}}{\partial \eta} + \left(3\Phi_0^{(i)2}\Phi_1^{(i)} - \Phi_1^{(i)} - \frac{\partial^2 \Phi_1^{(i)}}{\partial \eta^2}\right)\frac{\partial \Phi_0^{(i)}}{\partial \eta}\right], \tag{2.20a}$$

$$0 = \frac{\partial^2 \boldsymbol{u}_{\pi 0}^{(i)}}{\partial \eta^2}, \tag{2.20b}$$

$$0 = \frac{\partial^2}{\partial \eta^2}\left[\Phi_0^{(i)3} - \Phi_0^{(i)} - \frac{\partial^2 \Phi_0^{(i)}}{\partial \eta^2}\right]. \tag{2.20c}$$

The inner solution for the phase field is obtained as $\Phi_0^{(i)} = \tanh(\eta/\sqrt{2})$ by solving (2.20*c*) and matching with the external field $\Phi^{(e)} = \pm 1$. The inner profile is the same that one gets for an undisturbed interface. However, here the profile is expressed in terms of the normal coordinate η with the origin at the moving outer field discontinuity: the sharp interface. With respect to the sharp interface the inner phase field profile is sort of frozen.

It is important to stress that the equations for the inner layer (2.20) have been obtained under the strong, implicit assumption that a single time scale is involved in the dynamics. This assumption leads to the steady-state form of the equations, where time enters at most as a parameter. Later it will be shown that, under more general conditions, the inner profile needs to relax to the tanh profile from a generic initial state. The relaxation process will be found to be fast, corresponding to the existence of an inner time scale which recovers fast time derivatives in the inner layer equations. The general framework corresponds to a multiple time scale formalism such that $\partial/\partial t = \partial/\partial t_s + (M^*/Cn^3)\partial/\partial \tau$, where t_s is the slow external time (i.e. that considered up to now) and τ is the new, fast time variable. Clearly the ratio of the two time scales increases for vanishing Cahn number as $1/Cn$. For smooth evolutions from properly prepared initial data the fast scale is never activated, and the inner layer is slaved to the evolution of the external field while keeping the equilibrium tanh shape of the phase profile. In these conditions the expression for the leading order diffused capillary stress in (2.20*a*) simplifies considerably. Actually, since the tanh profile satisfies $(\Phi_0^{(i)3} - \Phi_0^{(i)} - \partial^2 \Phi_0^{(i)}/\partial \eta^2) = 0$, by using the identity

$$\frac{\partial}{\partial \eta}\left[\left(\Phi_0^{(i)^3} - \Phi_0^{(i)}\right)\Phi_1^{(i)} - \frac{\partial \Phi_0^{(i)}}{\partial \eta}\frac{\partial \Phi_1^{(i)}}{\partial \eta}\right] = \left[\left(3\Phi_0^{(i)^2} - 1\right)\Phi_1^{(i)} - \frac{\partial^2 \Phi_1^{(i)}}{\partial \eta^2}\right]\frac{\partial \Phi_0^{(i)}}{\partial \eta} + \left(\Phi_0^{(i)3} - \Phi_0^{(i)} - \frac{\partial^2 \Phi_0^{(i)}}{\partial \eta^2}\right)\frac{\partial \Phi_1^{(i)}}{\partial \eta}, \tag{2.21}$$

https://doi.org/10.1017/jfm.2012.461 Published online by Cambridge University Press

(2.20*a*) can be rewritten as

$$0 = -\frac{\partial p_0^{(i)}}{\partial \eta} + \frac{1}{Re}\frac{\partial}{\partial \eta}\left(\frac{1}{Cn}\frac{\partial u_{n0}^{(i)}}{\partial \eta}\right) - \frac{3}{2\sqrt{2}}\frac{C_\alpha^\alpha}{We}\left(\frac{\partial \Phi_0^{(i)}}{\partial \eta}\right)^2 + \frac{3}{2\sqrt{2}}\frac{1}{We}\frac{\partial}{\partial \eta}\left[\left(\Phi_0^{(i)3} - \Phi_0^{(i)}\right)\Phi_1^{(i)} - \frac{\partial \Phi_0^{(i)}}{\partial \eta}\frac{\partial \Phi_1^{(i)}}{\partial \eta}\right]. \tag{2.22}$$

We are now ready to recover the classical result which states that the tanh profile provides the correct capillary stress across the interface, resulting in a concentrated surface tension for the outer solution. This is the crucial technical point: among the different possible choices of the expansion parameter, selecting M^* such that $M^* \propto Cn^2$ leads to the formal identification of the distinguished limit as that which provides the correct surface tension to the external solution. This result could be interpreted by saying that, as the distributed interface thickness decreases, the mobility should be tuned to keep dynamic coupling with the external solution in the form of a concentrated force proportional to the interface curvature. Actually, integrating the normal component of the momentum equation (2.22) across the distributed interface and exploiting the tanh profile we readily obtain the Young–Laplace relation:

$$[[p_0^{(e)}]] = \frac{1}{Re}\left[\left[\frac{\partial u_{n0}^{(e)}}{\partial \zeta}\right]\right] - \frac{C_\alpha^\alpha}{We}, \tag{2.23}$$

where the last term in (2.22) vanishes upon integration due to the matching conditions $\Phi_0^{(i)}(\eta = \pm\infty) = \Phi_0^{(e)}(0^\pm) \equiv \pm 1$ and the Young–Laplace term proportional to curvature appears as a result of the known property of the tanh profile,

$$\frac{3}{2\sqrt{2}}\int_{-\infty}^{\infty}\left[\frac{\mathrm{d}\Phi_0^{(i)}}{\mathrm{d}\eta}\right]^2 \mathrm{d}\eta = 1. \tag{2.24}$$

Completing the leading order solution is now straightforward. The general solution of the tangent component of the momentum equation (2.20*b*) is $\boldsymbol{u}_{\pi 0}^{(i)} = \boldsymbol{a}\eta + \boldsymbol{b}$. Matching with a bounded outer solution,

$$\lim_{\eta \to \pm\infty} \boldsymbol{u}_{\pi 0}^{(i)} = \lim_{\zeta \to 0^\pm} \boldsymbol{u}_{\pi 0}^{(e)}, \tag{2.25}$$

yields $\boldsymbol{a} = 0$. Hence, to leading order, the inner profile of tangential velocity is uniform across the layer and the jump in the tangential component of the outer velocity vanishes,

$$[[\boldsymbol{u}_{\pi 0}]] = 0. \tag{2.26}$$

Since the velocity is uniform no tangential stress occurs in the inner layer, entailing the continuity across the interface of the tangential stresses of the outer solution

$$\left[\left[\frac{\partial \boldsymbol{u}_{\pi 0}}{\partial \zeta}\right]\right] = 0. \tag{2.27}$$

The leading order solution is now complete. Having recovered the correct sharp-interface limit, we conclude that the proper choice for the unknown mobility parameter is indeed $M^* \propto Cn^2$. Actually (2.12) with the jump conditions (2.18), (2.26) and (2.27) and the Young–Laplace equation (2.23) is the classical description of a sharp

https://doi.org/10.1017/jfm.2012.461 Published online by Cambridge University Press

interface between two immiscible fluids, $\Phi_0^{(e)} = \pm 1$. It is immediately realized that no other choice leads to the correct and consistent result. For instance, $M^* \propto Cn^4$ would make the identification of a common expansion parameter for inner and outer field impossible, thereby hampering the matching procedure.

It is worth stressing that the scaling we have found corresponds to $M \propto 2\sqrt{2}/3\lambda\omega\ell^2/\sigma$ when expressed in dimensional variables. The expression involves external scale quantities, namely the length ℓ and the characteristic time $1/\omega$ which are set by the system configuration and are not properties of the fluids. We conclude that M is actually an effective flow-dependent parameter, rather than an intrinsic feature of the interface.

The expansion can be carried out to the next order but this point is skipped here, since the focus is in tuning the model in order to reproduce the interfacial dynamics for an interface which is indeed sharp, so that higher-order corrections are physically irrelevant. Before proceeding to the validation of the results by numerical computations, we would like to stress that, once suitable values of M^* and Cn, small but finite, are selected to numerically model a specific flow, the inner layer dynamics is kept alive in the complete diffuse-interface model (2.4). This crucial property can then be exploited to allow topological changes of the interface while retaining the correct interfacial dynamics away from such singular events, a feature of paramount importance in many cases.

2.3. *Energetics and the singularity in the dissipation*

In the previous subsection the sharp-interface limit was derived by implicitly assuming an evolution on the time scale of the external solution, $1/\omega$. In fact, as anticipated, a faster time scale τ may be excited by the dynamics of the inner layer. The physical interpretation is that excess free energy stored in the interface needs to be dissipated to relax the inner phase profile to the tanh shape in local adiabatic equilibrium with the external conditions. The conclusions reached in § 2.2 remain substantially unaltered, although some more information concerning the energetics of the system is needed for a complete analysis of the fast time dynamics.

The total free energy of the system, sum of the thermodynamic free energy equation (2.2) and kinetic energy, made dimensionless with respect to the reference energy $\rho U^2 L^3$, is

$$F_T[\Phi, \boldsymbol{u}] = \int_\Omega \left\{ \frac{3}{2\sqrt{2}} \frac{Cn}{We} \left[\frac{\left(\Phi^2 - 1\right)^2}{4Cn^2} + \frac{1}{2} |\boldsymbol{\nabla}\Phi|^2 \right] + \frac{1}{2} |\boldsymbol{u}|^2 \right\} \mathrm{d}V. \tag{2.28}$$

Its time derivative follows as

$$\dot{F}_T[\Phi, \boldsymbol{u}] = \int_\Omega \left(\frac{\delta F_T}{\delta \Phi} \dot{\Phi} + \frac{\delta F_T}{\delta \boldsymbol{u}} \cdot \dot{\boldsymbol{u}} \right) \mathrm{d}V = \int_\Omega \left(\frac{3}{2\sqrt{2}} \frac{1}{We\, Cn} \mu_c \dot{\Phi} + \boldsymbol{u} \cdot \dot{\boldsymbol{u}} \right) \mathrm{d}V, \tag{2.29}$$

where the non-dimensional chemical potential is $\mu_c = \Phi^3 - \Phi - Cn^2 \nabla^2 \Phi$. Exploiting the balance equations (2.4*b*) and (2.4*c*), the time derivative of the total free energy is then

$$\begin{aligned} \dot{F}_T[\Phi, \boldsymbol{u}] = & \int_\Omega \left(\frac{3}{2\sqrt{2}} \frac{M^*}{We\, Cn^2} \boldsymbol{J} \cdot \boldsymbol{\nabla} \mu_c - \frac{1}{Re} \boldsymbol{\Sigma} : \boldsymbol{\nabla} \boldsymbol{u} \right) \mathrm{d}V \\ & + \int_{\partial\Omega} \left(-\frac{3}{2\sqrt{2}} \frac{M^*}{We\, Cn^2} \mu_c \boldsymbol{J} \cdot \boldsymbol{n} + \boldsymbol{u} \cdot \boldsymbol{t} - \frac{1}{2} |\boldsymbol{u}|^2 \boldsymbol{u} \cdot \boldsymbol{n} \right) \mathrm{d}S, \end{aligned} \tag{2.30}$$

https://doi.org/10.1017/jfm.2012.461 Published online by Cambridge University Press

where $\boldsymbol{t} = \boldsymbol{T} \cdot \boldsymbol{n}$, with $\boldsymbol{T} = -p\boldsymbol{I} + \boldsymbol{\Sigma}/Re$, p is the pressure and $\boldsymbol{\Sigma} = (\boldsymbol{\nabla u} + \boldsymbol{\nabla u}^{\mathrm{T}})$ is twice the deformation velocity tensor. For the boundary conditions that will be explicitly considered (unbounded domain) the surface integral vanishes and the dissipation inequality following from the second principle of thermodynamics takes the form

$$\dot{F}_T[\Phi, \boldsymbol{u}] = \int_\Omega \left(\frac{3}{2\sqrt{2}} \frac{M^*}{We\, Cn^2} \boldsymbol{J} \cdot \boldsymbol{\nabla} \mu_c - \frac{1}{Re} \boldsymbol{\Sigma} : \boldsymbol{\nabla u} \right) \mathrm{d}V \leqslant 0. \tag{2.31}$$

Two entropic mechanisms characterize the system, one associated with mechanical energy dissipation and the other with the relaxation of interfacial chemical energy, a negative-definite contribution in itself since $\boldsymbol{J} = -\boldsymbol{\nabla} \mu_c$.

The overall chemical free energy dissipation rate written in inner variables, together with the prescription $M^* = Cn^2$, reads as

$$\Pi_c^{(i)} = \int_{\mathscr{A}} \int_{-\infty}^{+\infty} -\frac{3}{2\sqrt{2}} \frac{1}{We\, Cn} \left[\frac{\partial}{\partial \eta} \left(\Phi^{3(i)} - \Phi^{(i)} - \frac{\partial^2 \Phi^{(i)}}{\partial \eta^2} \right) \right]^2 \mathrm{d}\eta\, \mathrm{d}S, \tag{2.32}$$

where $\mathscr{A}$ is the interface surface, $\mathrm{d}V = Cn\, \mathrm{d}\eta\, \mathrm{d}S$ and $\boldsymbol{\nabla} \simeq 1/Cn \partial/\partial \eta \boldsymbol{n}$. It is then apparent that the chemical dissipation rate diverges in the limit of vanishing interface thickness, $Cn \to 0$, unless the integrand vanishes (tanh profile). However, the physically relevant quantity is the total dissipation, rather than the dissipation rate. Assuming that the available amount of energy is finite, the total dissipation occurring up to time t_0 should remain finite,

$$\lim_{Cn \to 0} \int_0^{t_0} \Pi_c \, \mathrm{d}t = \text{const.} \tag{2.33}$$

It follows that the dissipation has to act on the fast time scale $\tau = t/Cn$, in such a way that

$$\lim_{Cn \to 0} \int_0^{t_0/Cn} \int_{\mathscr{A}} \int_{-\infty}^{+\infty} -\frac{3}{2\sqrt{2}} \frac{1}{We} \left[\frac{\partial}{\partial \eta} \left(\Phi^{3(i)} - \Phi^{(i)} - \frac{\partial^2 \Phi^{(i)}}{\partial \eta^2} \right) \right]^2 \mathrm{d}\eta\, \mathrm{d}S\, \mathrm{d}\tau = c_0, \tag{2.34}$$

where $c_0 < \infty$ is a constant depending on t_0. We see that the integrand must be a rapidly decreasing function of the fast time scale τ in order to keep the dissipation finite. Equation (2.34) holds for any t_0, however small, and the integrand substantially vanishes identically for $\tau > \tau_d$, for a finite τ_d. The conclusion is that such dissipation events are indeed extremely fast, occurring on a time scale order Cn at most in terms of the external time, $t_d = Cn\tau_d$. The chemical free energy dissipation event must be completed in a such small time interval, implying that the phase profile has meanwhile completed its relaxation to the equilibrium tanh shape.

The quantity $\Delta F = \lim_{t_d \to 0} \int_0^{t_d} \Pi_c \, \mathrm{d}t = \lim_{Cn \to 0} \int_0^{\tau_d} \Pi_c Cn \, \mathrm{d}\tau$ is the amount of free energy dissipated during the abrupt inner profile relaxation. Since the tanh profile does not involve dissipation, $\mu_c[\tanh(\zeta/\sqrt{2}Cn)] \equiv 0$, once the equilibrium profile is achieved no more singular events of this kind are expected, unless forced by abrupt (fast) events such as topological changes.

It is important to stress that (2.33) and (2.34) express asymptotic features emerging in the limit of small Cahn number. In principle the chemical dissipation rate $Cn\Pi_c$ may even assume a self-similar time behaviour taking the form of a Cahn-independent function of the fast time τ. In most cases time self-similarity is not achieved. Nevertheless dissipative event associated with the inner phase profile dynamics must

https://doi.org/10.1017/jfm.2012.461 Published online by Cambridge University Press

occur on the fast time scale, i.e. on a time interval shrinking to zero as the Cahn number is reduced.

The existence of a fast time scale requires to partially rearrange the asymptotic expansion. In particular, after introducing the two time scale expansion $\Phi = \Phi(\eta, t_s, \tau)$ and the prescription $M^* = Cn^2$, the leading order term of (2.13*d*) for the inner profile becomes

$$\frac{\partial \Phi_0^{(i)}}{\partial \tau} = \frac{\partial^2}{\partial \eta^2}\left(\Phi_0^{3(i)} - \Phi_0^{(i)} - \frac{\partial^2 \Phi_0^{(i)}}{\partial \eta^2}\right). \tag{2.35}$$

The system (2.20) is recovered for $\tau \gg 1$, a condition always verified on the external time scale for vanishing Cahn number. The consequence of (2.35) is that, at leading order and under the assumption of a smooth curvature radius, the fast time evolution of the inner profile becomes Cn-independent in the limit. Consistently also the inner layer free energy and rescaled chemical dissipation become Cn-independent,

$$F(\tau) = \frac{3}{2\sqrt{2}}\frac{1}{We}\int_{\mathscr{A}}\int_{-\infty}^{\infty}\left[\frac{\left(\Phi(\tau)^2 - 1\right)^2}{4} + \frac{1}{2}\left(\frac{\partial \Phi\,(\tau)}{\partial \eta}\right)^2\right] \mathrm{d}\eta\,\mathrm{d}S, \tag{2.36}$$

and

$$Cn\,\Pi_c(\tau)^{(i)} = \int_{\mathscr{A}}\int_{-\infty}^{+\infty} -\frac{3}{2\sqrt{2}}\frac{1}{We}\left[\frac{\partial}{\partial \eta}\left(\Phi(\tau)^{3(i)} - \Phi\,(\tau)^{(i)} - \frac{\partial^2 \Phi(\tau)^{(i)}}{\partial \eta^2}\right)\right]^2 \mathrm{d}\eta\,\mathrm{d}S. \tag{2.37}$$

It is worthwhile stressing that the kinetic energy, instead, does not respond on the fast time τ. The consequence is that a Young–Laplace-like jump condition holds across the interface also during the fast relaxation phase. The argument is briefly illustrated below. Owing to the matching conditions, the existence of a fast velocity response in the inner layer would lead to a corresponding fast response of the external field and to a singularity in the acceleration and the pressure gradient, see (2.12*b*). This singular response of the external field is excluded by physical assumption. Actually, the equation for the inner layer normal velocity (2.13*b*) can be rearranged as

$$\frac{\delta v_n}{\delta t} = -\frac{1}{Cn}\frac{\partial \tilde{p}_0^{(i)}}{\partial \eta} + \frac{1}{Re\,Cn}\frac{\partial}{\partial \eta}\left(\frac{1}{Cn}\frac{\partial u_{n0}^{(i)}}{\partial \eta}\right) - \frac{3}{2\sqrt{2}}\frac{C_\alpha^\alpha}{We\,Cn}\left(\frac{\partial \Phi_0^{(i)}}{\partial \eta}\right)^2, \tag{2.38}$$

where the modified pressure,

$$\tilde{p}_0^{(i)} = p_0^{(i)} + \frac{3}{2\sqrt{2}}\frac{1}{We\,Cn}\left[\frac{(\Phi_0^{(i)2} - 1)^2}{4} - \frac{1}{2}\left(\frac{\partial \Phi_0^{(i)}}{\partial \eta}\right)^2\right], \tag{2.39}$$

includes gradient-type contributions from the distributed capillary force. In these conditions, either the right-hand side of (2.38) vanishes identically, or a fast time scale response of the interface velocity occurs, $\delta v_n/\delta t = O(1/Cn)$. Once the singularity implied by the second case is ruled out, the consequence is the vanishing of the right-hand side of (2.38). From this a Young–Laplace-like jump condition is readily obtained by integrating (2.38) across the layer,

$$[[p_0^{(e)}]] = \frac{1}{Re}\left[\left[\frac{\partial u_{n0}^{(e)}}{\partial \zeta}\right]\right] - \frac{C_\alpha^\alpha}{We}\sigma^*, \tag{2.40}$$

https://doi.org/10.1017/jfm.2012.461 Published online by Cambridge University Press

where the order-one coefficient

$$\sigma^* = \int_{-\infty}^{+\infty} \frac{3}{2\sqrt{2}} \left(\frac{\partial \Phi^{(i)}}{\partial \eta} \right)^2 \mathrm{d}\eta \tag{2.41}$$

relaxes towards one on the fast time scale together with the equilibrium tanh profile. After the relaxation is completed no other singular event occurs and the inner layer keeps on staying in adiabatic equilibrium with the outer solution (slaved inner profile), until a new singular event is triggered by, e.g., topological changes such as drop coalescence and breakdown.

In conclusion, any solution of the Cahn–Hilliard/Navier–Stokes problem with smooth external field satisfies a Young–Laplace jump condition across the interface once the sharp-interface limit is taken. A singularly fast relaxation dynamics is instead expected to occur in the inner phase profile, corresponding to the abrupt dissipation of the excess chemical free energy stored in the interfacial layer.

2.4. *Capillary waves*

A well-known feature of the sharp-interface model is its ability to support the propagation of capillary waves, where the interface oscillates about its unperturbed, planar configuration as a result of the interplay between kinetic energy of the two fluid phases and internal energy of the perturbed interface (Lighthill 2001). The problem is well known and is reviewed here for the reader convenience since the results will be used as one of the benchmarks for our numerical data.

At low Reynolds number, dissipative effects in the two bulk phases are significant and the wave is progressively attenuated until it eventually disappears. The problem has been thoroughly addressed in the literature and the classical approach consists of solving an eigenvalue problem for the small-amplitude linearized system given by the Stokes equations in the two bulk phases and the jump conditions across the undisturbed position of the interface. The parameter of the eigenvalue problem is the wavelength of the wave, here assumed planar, and the eigenvalue is the complex frequency whose real and imaginary parts are the circular frequency and the damping rate, respectively. The dispersion relationship can be worked out analytically (Jeng *et al.* 1998) and for two bulk phases with matching density and viscosity is given by

$$(k - l) \left[\omega(k)^2 - \frac{\sigma k^3}{2\rho} \right] - k\omega(k)^2 = 0, \tag{2.42}$$

with $k = 2\pi/\lambda$ the wavenumber and $l = k\sqrt{1 - \mathrm{i}\omega(k)/(\nu k^2)}$. By equating to zero the terms in square brackets provides the dispersion relationship for the inviscid case. The expression of the free-surface elevation as a function of time has been obtained by Prosperetti (1981), and is too cumbersome to be repeated here.

The two-dimensional analytic solution of Prosperetti (1981) for small-amplitude capillary waves is used in the next section as a benchmark for the diffuse-interface model to check its ability in reproducing the sharp-interface dynamics as the Cahn number is decreased. The effect of changing the mobility parameter is addressed to validate the predicted scaling law for the mobility, $M^* \propto Cn^2$. Clearly the numerical simulations are carried out at finite Cahn number and wave steepness $\delta = A/\lambda$, with A the wave amplitude. In comparing the numerical results with the analytical solution several wave amplitudes were tested to ensure that the model worked in the linear range. It should be emphasized that the order in which limits are taken matters: we have to deal with the zero-wave-amplitude limit of the zero-thickness asymptotics of

https://doi.org/10.1017/jfm.2012.461 Published online by Cambridge University Press

the Cahn–Hilliard model. Hence, the wave amplitude should always be larger than the interface thickness $\ell/A = Cn/\delta < 1$. We recall that the nominal interface position to be compared with the sharp-interface theory is taken to coincide with the zero isoline of the phase field, $\Phi(x, z, t) = 0$. The explicit equation of the nominal surface is $z_I = z_I(x, t)$ and, consistently, the velocity component normal to the unperturbed interface is defined as $w_I = \dot{z}_I(x, t)$.

3. Numerical experiments and validation

3.1. *Numerical algorithm*

The system of (2.4) has been discretized by finite differences on a staggered and uniform grid using central second-order approximations. The time integration is performed with a semi-implicit scheme: the linear part of the system is treated implicitly by the use of a classical Crank–Nicolson second-order approximation; on the other hand, a four-stage, third-order, low-storage Runge–Kutta scheme is used for the nonlinear part. For the prototypical differential equation $\partial f/\partial t = \boldsymbol{L}[f] + \boldsymbol{N}[f]$, the scheme reads

$$\left(\boldsymbol{I} - \frac{\Delta t}{2}(\alpha_i + \beta_i)\boldsymbol{L}\right)[f^{n+1}] = f^n + \Delta t\beta_i \boldsymbol{N}[f^{n-1}] + \frac{\Delta t}{2}(\alpha_i + \beta_i)\boldsymbol{L}[f^n] + \Delta t\alpha_i \boldsymbol{N}[f^n], \quad (3.1)$$

with $\boldsymbol{L}[\cdot]$ and $\boldsymbol{N}[\cdot]$ the discretized version of the linear and the nonlinear part of the system, respectively, and α_i and β_i the Runge–Kutta coefficients of the i th step. Special attention is devoted to the solution of the Cahn–Hilliard equation which is based on the semi-implicit splitting proposed by Vollmayr-Lee & Rutenberg (2003). In this case, $\boldsymbol{L}[\cdot]$ and $\boldsymbol{N}[\cdot]$ in (2.4*c*) are

$$\boldsymbol{L}[\Phi] = \tau\frac{M^*}{Cn}\mathrm{D}^2[\Phi] - Cn\,M^*\mathrm{D}^4[\Phi] \quad (3.2a)$$

$$\boldsymbol{N}[\Phi] = \frac{M^*}{Cn}[\mathrm{D}^2[\Phi^3] - (1+\tau)\mathrm{D}^2[\Phi]] - u_x\mathrm{D}_x[\Phi] - u_y\mathrm{D}_y[\Phi], \quad (3.2b)$$

with $\tau = 2$ as suggested in Badalassi *et al.* (2003), $\mathrm{D}_x[\cdot]$, $\mathrm{D}_y[\cdot]$, $\mathrm{D}^2[\cdot]$, $\mathrm{D}^4[\cdot]$ the discretized version of the continuum operators $\partial/\partial x$, $\partial/\partial y$, ∇^2 and ∇^4, respectively, and u_x, u_y the two velocity components. The incompressible Navier–Stokes equations are solved with a classical projection method on a staggered grid. This numerical scheme has been applied to planar standing capillary waves (two-dimensional problem) of wavelength λ at the fluid–fluid diffuse interface in the 'deep layer' approximation (formally the deep layer approximation requires $H/2 \gg \lambda/2\pi$, with $H/2$ the depth of the two fluid regions separated by the interface, in fact $H/(2\lambda) = 1$ is sufficient).

The system consists of two superimposed layers of two immiscible fluids, $\Phi = \pm 1$, assumed for simplicity with identical density and viscosity, lighter and darker tones (red and blue in the electronic version, respectively) in figure 2(*a*). The two fluid layers are confined between two planar, parallel, impermeable walls at $z = -H/2$ and $z = H/2$ where adherence conditions are enforced for the velocity. Since the distance between interface and solid walls is significantly larger than the wavelength, the exponential cut-off, $\boldsymbol{u} \propto \mathrm{e}^{-2\pi|z|/\lambda}$, makes the velocity field already vanish well ahead the position of the walls. As a consequence, to any practical respect, the walls do not alter the field with respect to the infinite layer depth case. Concerning the phase, the boundary conditions at the solid walls are

$$\frac{\partial \Phi}{\partial n} = 0, \quad (3.3)$$

https://doi.org/10.1017/jfm.2012.461 Published online by Cambridge University Press

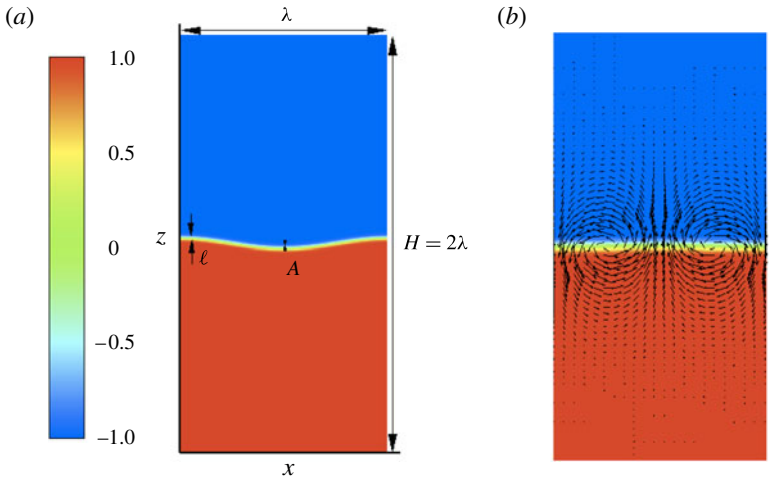


FIGURE 2. (Colour online) (*a*) Sketch of the system, a standing capillary wave of wavelength λ and amplitude A rides the interface of thickness ℓ; lighter and darker tones (red and blue in the online version) denote the two pure fluids $\Phi = 1, -1$, respectively. (*b*) Visualization of the velocity field at time $t/2\pi = 0.26$ of maximum fluid kinetic energy when the interface is flat. Only a few vectors are shown to convey an impression on the structure of the field while avoiding blurring the image. The relevant parameters are $Cn = 0.02$, $\delta = A/\lambda = 0.025$ and $M^* = 3Cn^2$.

$$\boldsymbol{J}\cdot\boldsymbol{n} = M\frac{\partial}{\partial n}[3\sigma(\Phi^3 - \Phi - \ell^2\nabla^2\Phi)/(2\sqrt{2}\ell)] = 0. \tag{3.4}$$

While the second condition straightforwardly implies that there is no phase-flux across the solid wall, the first condition directly follows from the boundary terms in the free energy functional (2.2), where the boundary potential is prescribed as $f_w = -1/4\sigma\cos(\theta_e)\Phi(3-\Phi^2)+(\sigma_{w1}+\sigma_{w2})/2$. The complete discussion of the boundary conditions for the phase field is beyond the scope of this work, see Seppecher (1996), Jacqmin (2000), Carlson, Do-Quang & Amberg (2009) and Yue *et al.* (2010). In order to provide a few more details, θ_e in the boundary potential is the equilibrium contact angle at a triple line where the interface between the two fluid phases intercepts the solid boundary. This event never occurs in the present case, hence we took the freedom to select $\theta_e = 90°$, an inconsequential choice which simplifies the expression of the wall potential to $f_w = (\sigma_{w1} + \sigma_{w2})/2$, with $\sigma_{w1,2}$ the surface tensions between any of the phases and the solid. It is worth stressing that the asymptotic behaviour of the Cahn–Hilliard equation in the presence of an asymptotically vanishing velocity guarantees that Φ approaches ± 1 on the two sides of the interface sufficiently fast to identically satisfy the boundary conditions. Hence, here equations (3.3) and (3.4) take the role of an easy and effective prescription of the far field behaviour of the field.

The initially flat interface at $z = 0$ is perturbed by a monochromatic, sinusoidal displacement with wavelength λ and amplitude $\delta = A/\lambda = 2.5 \times 10^{-2}$, which allows using periodic boundary conditions in the x direction. The tests presented here are mainly performed by changing the Cahn number Cn and the mobility factor M^*, at fixed Reynolds and Weber number, $Re = 2500$ and $We = 4\pi^3$, respectively. We recall that combining the definition of Weber number, $We = \rho U^2\lambda/\sigma$ with $U = \lambda\omega$, and the inviscid dispersion relation, $\omega^2 = \sigma\,(2\pi)^3/(2\lambda^3\rho)$, the Weber number follows as

https://doi.org/10.1017/jfm.2012.461 Published online by Cambridge University Press

$We = 4\pi^3 = \text{const}$. To complete the basic picture, a brief account of the effect of changing Reynolds number and wave amplitude A or wave steepness $\delta = A/\lambda$ will also be provided in connection with the discussion of our main results reported in figure 4. In the data discussed here, the ratio of nominal interface thickness ℓ to grid size Δz is always fixed to $\ell/\Delta z \simeq 8$ which corresponds to $\sim$30 grid points within the actual thickness of the interface. Indeed, as stated in Jacqmin (1999), 98.5 % of the surface tension is contained in the layer where the phase ranges from -0.9 to $+0.9$. The thickness of this layer is $\hat{\ell} \approx 4.\ell$, implying that the ratio $\ell/\Delta z \simeq 8$ corresponds to having 32 points inside the actual diffused interface. Preliminary tests showed that the ensuing grid accurately resolves all of the relevant length scales. It could have well been significantly coarsened if our purpose was limited to reproducing the dynamics of the system at finite interface thickness rather than assessing the approach to the sharp-interface behaviour. Actually the asymptotic analysis of § 2.2 shows that the inner layer velocity field becomes constant in the zero-Cahn-number limit, and what actually matters is the reasonably accurate resolution of the tanh profile of the zeroth-order inner layer phase field. Resolution requirements in the direction of wave propagation are clearly less stringent, here $\Delta x/\Delta z$ is in the range 4–6.

3.2. *Cahn number effect on capillary dynamics and the optimal mobility*

Starting with the perturbed phase field, the capillary stress provided by the initial curvature induces the oscillation of the interface. The time evolution of the nominal interface velocity w_I (at $x = \lambda/2$, maximum standing wave amplitude) is reported in figure 3(*a*) at changing Cn. The mobility parameter has been assumed as $M^* = 6Cn^2$. The proportionality factor 6 is different from what will be shown to be the optimal ($M^*_{opt} = 3Cn^2$) to make the three curves in the plot easily distinguishable. In the same figure the analytical solution w_a obtained by Prosperetti (1981) for the sharp-interface model of capillary waves is reported to provide reference data. The difference between the numerical and the analytical solutions slightly increases with time and, as expected, the agreement gets better by reducing the Cahn number. The accuracy is quantified by the relative global error $Err = \|w_I - w_a\|/\|w_a\|$, where $\|\cdot\|$ denotes the L_2-norm over the oscillation period $T = 2\pi/\omega$. We observe a good agreement starting from $Cn = 0.01$ (squares in figure 3*a*) with a global error of $\sim$5.6 %, in line with previous results (Jacqmin 2000). In figure 3(*b*) we compare the outer profile of the normal velocity component $w(\zeta)$, now using the mobility $M^*_{opt}(Cn)$ which yields the best agreement with the reference solution. The selected dimensionless time instant and position, $t/(2\pi) = 0.26$ and $x = 1/2$, respectively, correspond to peak oscillation amplitude, see the left panel of the same figure. The outer profile actually shown in the right panel is the zero-Cahn-number extrapolation $w_0^{(e)}$ of the data pertaining to three different simulations at progressively reduced Cahn number. More details are provided in Appendix.

We are now ready to discuss how the mobility parameter M^* affects the dynamics of the interface to validate the asymptotic theory of § 2.2. As already commented, selecting the appropriate value for M^* is a delicate issue. The theory suggests using a scaling of the form $M^* = \alpha Cn^2$ as the only correct procedure to approach the limit of vanishing Cahn number while retaining the known dynamics of a sharp interface between immiscible fluids. The specific value of the proportionality constant α is irrelevant for reaching the proper distinguished limit. However, it could bear practical importance for numerical algorithms aimed at simulating the sharp interface with a finite, practically affordable resolution.

https://doi.org/10.1017/jfm.2012.461 Published online by Cambridge University Press

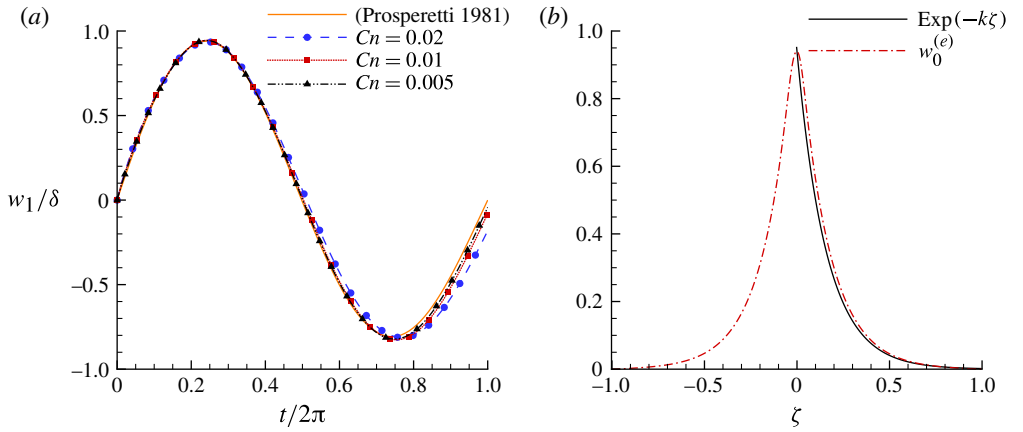


FIGURE 3. (Colour online) Standing capillary wave: $\delta = A/\lambda = 0.025$. (*a*) Interface velocity w_I at $x = 1/2$ (dimensionless position of maximum standing wave oscillation) versus dimensionless time t for different Cahn numbers and $M^* = 6Cn^2$. Data are compared with the analytical solution of the sharp-interface model (Prosperetti 1981). Since the system is dissipative, the oscillation amplitude decreases in time. The dimensionless interface velocity is scaled with the dimensionless wave amplitude δ. (*b*) Dimensionless outer normal fluid velocity distribution $w(\zeta)$ across the interface versus outer scale distance ζ from the interface at time $t/2\pi = 0.26$ and position $x = 1/2$ of peak wave oscillation. In fact (see Appendix), the velocity distribution shown by the dashed line is the extrapolation to zero interface thickness, $w_0^{(e)}(\zeta) = \lim_{Cn\to 0} w(\zeta, Cn)$, of the data for $M^*_{opt} = 3Cn^2$ (the optimal mobility, § 3.2) and the same progressively smaller Cahn numbers reported in the legend of (*a*). The solid line is the analytical distribution.

Figure 4(*a*) shows the time evolution of the vertical interface velocity at the position of maximum standing wave amplitude, $x = 1/2$ changing M^* at fixed $Cn = 0.02$. The initial condition used for the phase field is a linear profile adjoining the two bulk regions where $\Phi = \pm 1$ through an inner layer of thickness 2ℓ,

$$\Phi(x, \zeta, 0) = \begin{cases} -1 & \ell < \zeta \\ -\zeta/\ell & -\ell \leqslant \zeta \leqslant \ell \\ 1 & \zeta < -\ell. \end{cases} \tag{3.5}$$

This initial condition is particularly severe and has been devised as a test to check the model ability in recovering the equilibrium tanh profile and in reproducing the outer field of the wave. Adaptation of the inner profile is indeed common when strong nonlinear effects highly deform the interface or in the case of topology transitions. The relevance of the test is clear after considering that the capillary stress is related to the integral of $(\partial\Phi_0^{(i)}/\partial\eta)^2$ (see (2.24)). As a consequence, non-equilibrium profiles produce wrong surface tensions which may lead to large errors in the wave propagation.

Both the interface velocity (figure 4*a*, $M^* = 2.5 \times 10^{-7}$) and the wave period (not shown) experience large deviations with respect to the analytical predictions when M^* is too small. As will be shown later, such values of M^*, together with a non-equilibrium initial profile, hinder the correct evolution of the phase inside the interface, leading to incorrect results. Conversely when M^* is too large (figure 4*a*,

https://doi.org/10.1017/jfm.2012.461 Published online by Cambridge University Press

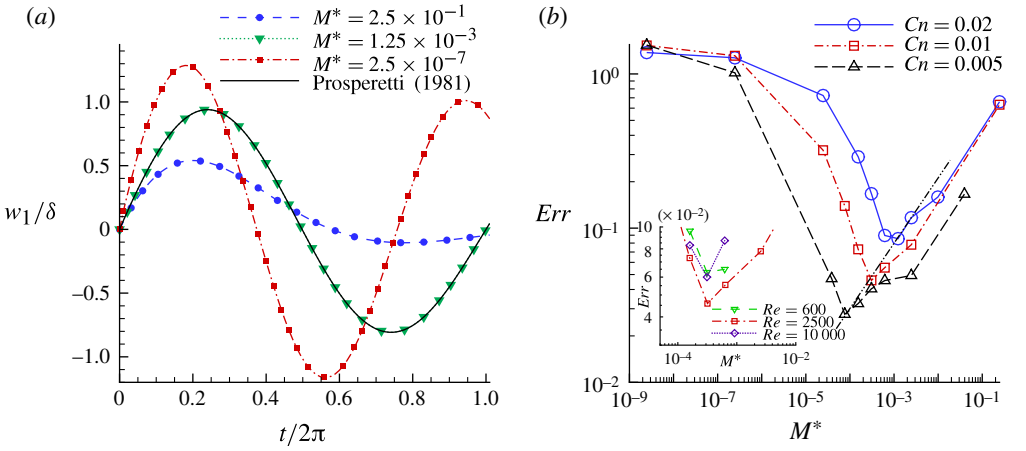


FIGURE 4. (Colour online) (*a*) Qualitative effects of the mobility on the time evolution of the interface normal velocity w_I at $x = \lambda/2$; the tests are performed with $Cn = 0.02$. (*b*) Global error $Err = \|w_I - w_a\|/\|w_a\|$ as a function of M^* at fixed Cahn number. Tests performed with a linear initial profile; the optimal mobility scales with the power law $M^*_{opt} = 3Cn^2$ (dash-dotted line). In the inset of (*b*) the error dependence on M^* at fixed $Cn = 0.01$ is shown for different Reynolds numbers. The optimal mobility M^*_{opt} is substantially unaffected by the Reynolds number.

$M^* = 2.5 \times 10^{-1}$), difficulties arise with the equation for the external solution. The reason is that the diffuse-interface model, at variance with its asymptotic form, keeps also in the external region the divergence of the phase flux $(M^*/Cn)\nabla \cdot \boldsymbol{J}$ which overwhelms the convection operated by the wave field $\mathrm{D}\Phi/\mathrm{D}t$ for large M^*. The equation tends to behave like $\nabla \cdot \boldsymbol{J} = 0$ and the phase field decouples from the velocity even if the inner phase profile equilibrates extremely fast. In these conditions the resulting diffused capillary stress alters the wave dynamics leading to the large error observed in the data denoted by circles. Optimal results are obtained by choosing $M^* = 1.25 \times 10^{-3}$, triangles in the figure, which perfectly match the analytical displacement velocity.

The discussion can be made more precise by quantifying the relative global error in the wave displacement velocity Err averaged over the first wave period. Figure 4(*b*) shows the error curves as a function of the mobility for three different Cahn numbers for the linear initial profile. The three curves have similar shape and are characterized by the optimal mobility $M^*_{opt}(Cn)$ which minimizes the error at given Cahn number. The optimal can be physically explained as the best compromise between two oppositely wrong solutions: too slow phase field evolution (small M^*) and velocity field decoupling from the phase field (large M^*). In correspondence of the optimal mobility $M^*_{opt}(Cn)$ the error decreases with the Cahn number, showing convergence towards the analytical, sharp-interface solution. Crucial feature of the diagrams in figure 4(*b*) is the shift of the minimum to the left with decreasing Cn (decreasing M^*_{opt}). Table 1 provides quantitative details. The data are consistent with a linear scaling of the error with the Cahn number, $Err \propto Cn$, as expected from the theory of § 2.2. Moreover, the theory predicts $M^* \propto Cn^2$. Indeed the optimal mobility data in the table can be accurately fit with the power law $M^*_{opt} = \alpha Cn^2$ with $\alpha \simeq 3$. Combining these ingredients yields $Err_{min} \propto \sqrt{M^*_{opt}}$ which is the dash-dotted straight

https://doi.org/10.1017/jfm.2012.461 Published online by Cambridge University Press

Cn	M^*_{opt}	Err (%)
0.02	1.25×10^{-3}	8.54
0.01	3.12×10^{-4}	4.58
0.005	7.81×10^{-5}	2.76

TABLE 1. Optimal mobility parameter M^*_{opt} and error $Err = \|w_I - w_a\|/\|w_a\|$ for different Cahn numbers. The error scales linearly with Cn for the optimal mobility $M^*_{opt} \simeq 3Cn^2$.

line adjoining the minima in the log–log plot in figure 4(*b*). Clearly, no claim of universality on the prefactor α can be avouched on the basis of this single data set. To provide more general information, the sensitivity of the error to the Reynolds number is summarized in the inset of figure 4(*b*), where evidence is produced of the substantial independence of M^*_{opt} on Re by providing data at fixed Cahn number $Cn = 0.01$ with three different Reynolds numbers, $Re = 600, 2500$ and $10\,000$. Additional simulations with a different steepness $\delta = A/\lambda = 0.0125$ produce indistinguishable results on the scale of the plot. For the reader's convenience, we recall that the information on the wave amplitude can be equivalently conveyed by introducing a suitably redefined Weber number, $\widehat{We} = \rho A^2 \lambda \omega^2/\sigma = 4\pi^3\delta^2$, which is given by the product of the Weber number already introduced and the square of the wave steepness.

So far we have discussed the behaviour of the interface on the time scale of the external wave, and we concluded that the mobility should be tuned in agreement with the theory of § 2.2 to reproduce the correct external dynamics. In fact, the inner field was shown to evolve on the fast time scale $\tau = tM^*/Cn^3$ in § 2.3.

Successive configurations of the inner phase profile are provided in figure 5(*a–c*) for different values of M^* at $x = 1/2$ for the same Cahn number of 0.02. The time reported in the legend is normalized with the external time scale set by the wave ($t^{(e)}$ in § 2.2). Given the Cahn number, a large mobility yields a quick equilibration of the inner profile which immediately relaxes to the equilibrium tanh shape. In figure 5(*a*) ($M^* = 2.5 \times 10^{-1}$) the inner profile is already relaxed to its final configuration by a time instant corresponding to 1/100th of the wave period. Although this may seem a good achievement, the corresponding curve in figure 4(*a*) (circles) shows the spoiling effect this large mobility has on wave dynamics. In contrast, a small value of M^* leads to a frozen inner phase profile.

Indeed figure 5(*c*) ($M^* = 2.5 \times 10^{-7}$) shows that the profile still retains its initial linear shape after more than one entire wave period is elapsed. Comparing with the corresponding plot in figure 4(*a*) (squares) it is clear that the dynamics of the wave is unduly altered. The case with optimal M^* is shown in figure 5(*b*) corresponding to the intermediate case at $M^* = 1.25 \times 10^{-3}$. With the optimal mobility the profile is able to relax to the equilibrium configuration fast enough to achieve the tanh shape in less than 1/10th of wave period for this case at $Cn = 0.02$. From the scaling of inner versus outer time scale, $\tau = tM^*/Cn^3$, it is clear that the equilibration time $t = \tau Cn^3/M^*$ shortens with the Cahn number when using the optimal mobility $M^*_{opt}(Cn) \propto Cn^2$. In general, the accuracy increases with reducing Cahn number when adopting the optimal prescription for the mobility (figure 4*b*), however the wave dynamics is already well reproduced at $Cn = 0.02$, curve shown by triangles in figure 4(*a*). For different mobilities, the profiles markedly differ when compared at fixed external time scale. They collapse to the same shape when the fast time scale τ is the same as

https://doi.org/10.1017/jfm.2012.461 Published online by Cambridge University Press

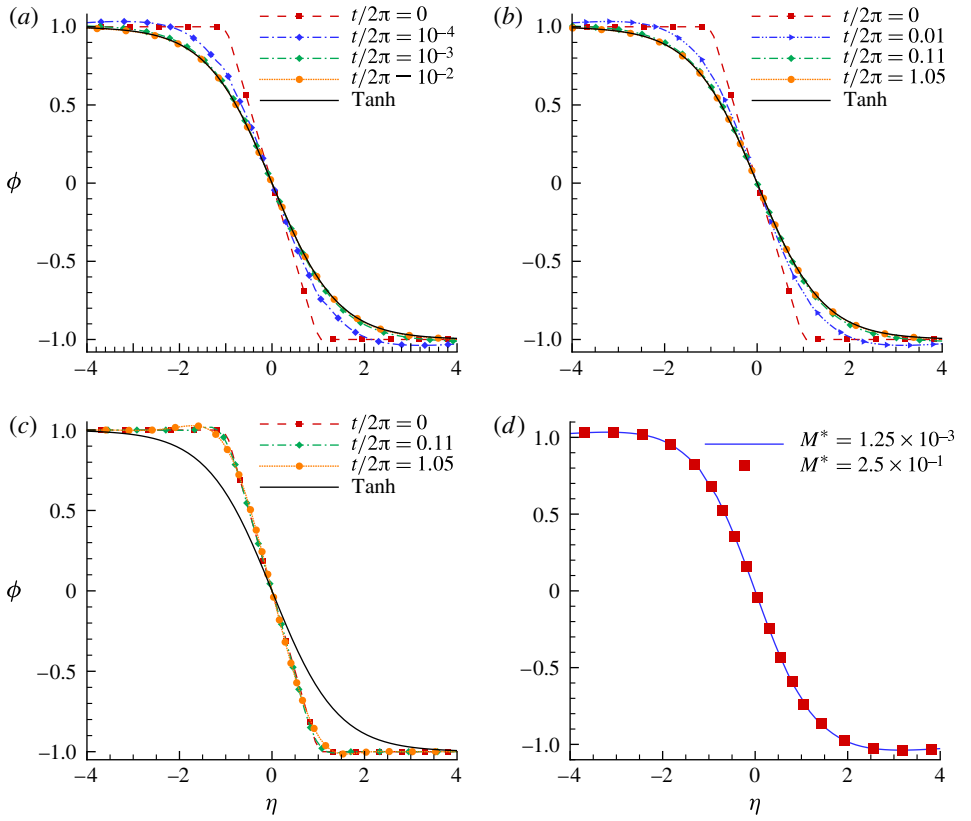


FIGURE 5. (Colour online) Inner profiles of the phase variable Φ versus distance from the nominal interface η at $Cn = 0.02$. (*a*) Fast equilibration, $M^* = 2.5 \times 10^{-1}$. (*b*) Optimal mobility, $M^* = 1.25 \times 10^{-3}$. (*c*) Extremely slow equilibration, $M^* = 2.5 \times 10^{-7}$. In the three legends time is given in external units. The solid line is the equilibrium tanh profile. (*d*) Inner phase profile at the same fast time $\tau = 3.25$ for two different mobility factors, see the legend.

shown in figure 5(*d*), where the two profiles correspond to two different mobilities M^* differing by about two orders of magnitude.

The fast time scale plays a key role in the analysis of global properties such as free energy and chemical dissipation, figure 6. Figure 6(*a*) we observe a faster free energy evolution for the solid curve (smaller Cahn number, $Cn = 0.005$) as compared with the dashed line ($Cn = 0.01$). The free energy can be read in the rescaled fast time $\tau = t/Cn$ in the upper x-axis (dashed curve and square symbols for $Cn = 0.01$ and $Cn = 0.005$, respectively). The curves perfectly match when expressed as functions of the fast time supporting the asymptotic theory (§ 2.3) which predicts from (2.36) Cn-independent free energy in the fast variable. A similar consideration holds for the chemical free-energy dissipation in figure 6(*b*). A steeper and faster evolution with reducing the Cahn number is expected by the theory and is shown in the figure. According to (2.37) we compare the rescaled chemical dissipation $Cn\,\Pi_c$ as a function of the fast time scale τ and again we obtain a perfect matching of the two curves (dashed curve and square symbols).

It is worth stressing once again that particularly severe initial conditions for the phase field were selected to provide stringent evidence of the agreement between

https://doi.org/10.1017/jfm.2012.461 Published online by Cambridge University Press

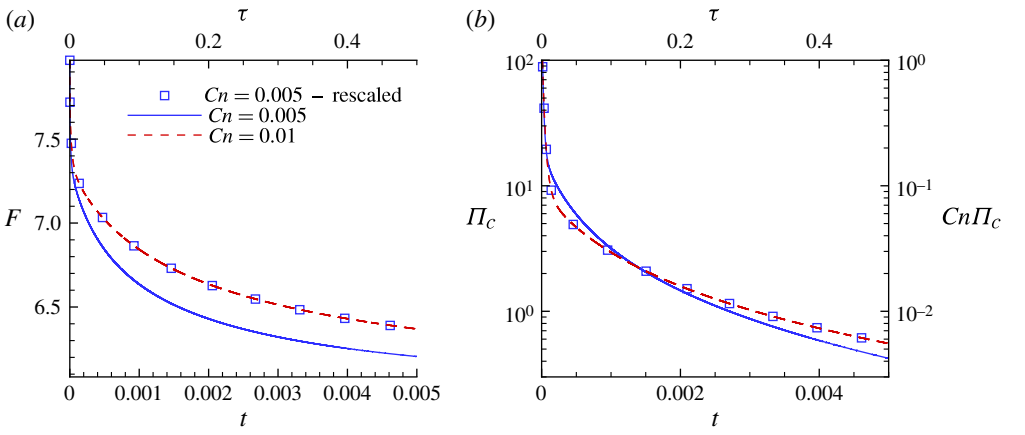


FIGURE 6. (Colour online) Fast and slow time evolution of the free energy (a) and of the chemical dissipation (b) during the very initial moments of the wave oscillation. Data are obtained using the prescription $M^* = Cn^2$. The solid and dashed curves are referred to the t-axis (bottom) and to the F and Π_c-axis, (a) and left axis in the right panel, respectively. The dashed curve can be simultaneously read also on the fast time τ-axis (top). In (a) the square symbols correspond to the same data of the solid curve, now plotted as functions of the fast time τ (top). In (b), the data on the fast time scale (dashed line and squares) must be read on the left $Cn\Pi_c$-axis where, again, the squares symbols and solid line correspond to the same (rescaled) data at $Cn = 0.005$, see the legend.

theoretical predictions and numerical experiments. It is clear that an initial tanh profile would have been sufficient in representing the correct behaviour in this simple problem. However, this choice would have hidden the role of the fast inner field equilibration necessary in the general case. Indeed the most interesting cases are actually those where the inner profile is forced far from equilibrium by strong interactions with the external field, as in cases where topology rearrangements occur. In these conditions a fast and accurate relaxation to the equilibrium tanh profile of the inner solution is mandatory to reproduce the correct surface tension and the subsequent dynamics.

For the sake of completeness, we also performed a comparison between two different initial conditions with a fixed Cahn number and different mobility parameter. The global error Err in the wave displacement velocity is plotted in figure 7. Squares and circles denote cases where the initial conditions are assigned as the tanh equilibrium profile and as the linear profile given in (3.5), respectively. The most significant feature of the plots is the minimum error which is comparable in the two cases and is achieved at the optimal mobility M^*_{opt}. Concerning the squares, it is apparent that reducing the mobility parameter below M^*_{opt} is irrelevant for the accuracy, which is indeed saturated since the correct inner profile was assigned from the beginning. On the other hand, the error for the circles increases when the mobility is below M^*_{opt}, since now the initial condition needs to equilibrate starting from a wrong initial guess. It is clear that the best general strategy consists in following the minimum located at $M^*_{opt}(Cn)$ at decreasing Cahn number, as explained in the discussion of figure 4(b). We observe that this strategy is indeed consistent with that proposed by Lowengrub & Truskinovsky (1998), who suggest $\lim_{Cn\to 0} M^*/Cn = 0$. Our result is more stringent, since we explicitly state the dependence of the mobility

https://doi.org/10.1017/jfm.2012.461 Published online by Cambridge University Press

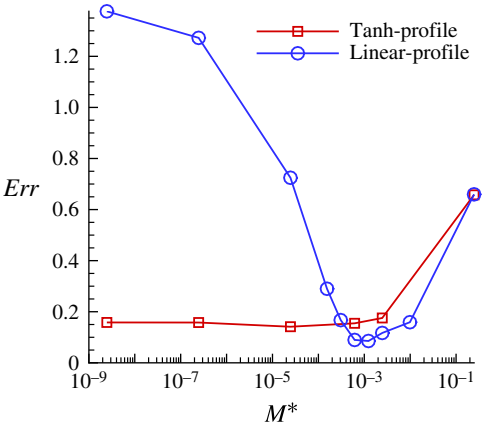


FIGURE 7. (Colour online) Wave displacement velocity error Err versus mobility M^* at $Cn = 0.02$ for two different initial phase profiles, see the legend.

parameter on the Cahn number as $M^* \propto Cn^2$. This optimal strategy, already explained as the best compromise between the two opposite requirements of fast relaxation to the equilibrium tanh profile and sensitiveness to the outer wave dynamics, becomes mandatory in the case of out-of-equilibrium transient conditions (e.g. rearrangement of interface topology).

3.3. *The effect of mobility in drop coalescence*

The previous section discussed the optimal mobility in the context of capillary wave propagation. By comparison with the available analytical solution, the theory discussed in § 2.2 has been validated showing that, indeed, convergence to the sharp-interface dynamics is achieved by selecting the mobility according to the scaling law $M^* \propto Cn^2$. Here we intend to demonstrate that the same prescription allows to correctly capture more interesting dynamics associated with topological changes of the interface.

As a prototypal problem we select the coalescence of two identical, cylindrical droplets, initially placed at small distance. The initial droplet radius is a, with the two centres at distance d along the x-axis. The nominal interface thickness is ℓ, and the Cahn number is $Cn = \ell/a$. The system is enclosed in a rectangular domain, with two solid walls parallel to the x-axis, far enough not to affect the evolution of the system, $2H \gg 2a$. Periodic conditions are used in the x-direction. When the initial separation falls below a critical distance, the two drops begin to interact to eventually coalesce and form a single drop with twice the initial volume. This problem is a simplified version of the head on collision of two droplets, dealt with in Yue *et al.* (2004), where their initial momentum makes the two droplets approach one another and squeeze between them a liquid film, the thickness of which decreases in time until coalescence.

Before discussing the results, it must be stressed that, in strict terms, the thin-layer asymptotics presented in § 2.2 cannot be applied to this configuration where small curvature radii, comparable with the interface thickness, develop during coalescence and the geometrical model of a thin layer with a well-defined normal and prevailing normal gradients ceases to exists during topology rearrangement. Indeed, strictly speaking, the theory applies to all time instants away from singular events (such as coalescence), when scale separation between normal and parallel directions to the

https://doi.org/10.1017/jfm.2012.461 Published online by Cambridge University Press

interface exists. In fact, the length scale parallel to the interface becomes comparable with the normal one during reconnection. In this phase we cannot trust the theory, since its basic assumptions are violated. Nevertheless, we are going to show through numerical experiments that the adoption of the criterion we propose still provides the proper balance between the fast and the slow time scales.

The problem is characterized by a typical inertial force $F_{in} \sim \rho U^2 a^2$, a viscous force $F_{vi} \sim \mu U a$ and a capillary force $F_{ca} \sim \sigma a$. The assumption $F_{ca} \simeq F_{vi}$, i.e. $Ca = \mu U/\sigma = 1$, pertains to the slow fluid motion regime. In this case the expected characteristic fluid velocity is $U = \sigma/\mu$, leading to $Re \equiv We = \rho\sigma a/\mu^2$. Fast fluid motion corresponds instead to balancing capillary and inertial forces, $We = 1$. Now the expected fluid velocity is $U = \sqrt{\sigma/(\rho a)}$, i.e. $Re = 1/Ca = \sqrt{\rho\sigma a}/\mu$. For the purpose of validation, our target is here a flow where significant fluid motion is induced by the capillary stress. Hence, a unitary Weber number is selected, $We = 1$, with $Re = 100$. Physically these parameters correspond to, e.g., $a = 5$ μm, $\sigma = 2 \times 10^{-2}$ N m^{-1}, $\rho = 10^3$ kg m^{-3} and $\mu = 10^{-1}$ kg (m s)$^{-1}$, such as for a 10 μm diameter oil (silicon oil, 100 cp) droplet in water, a binary system with negligible density difference and comparable viscosities.

The initial configuration of the two circular droplets (positive curvature $C = 1/a > 0$) is prescribed by the distance between the respective centres, $d = 2a(1 + 2Cn)$, in such a way that the two diffuse interfaces almost come into contact. Figure 8 shows successive configurations of the droplets for a case where $Cn = 0.1$, $H/a = 5$, $M^* = 0.01$ (only a small portion of the computational domain is shown and we are using $M^* = Cn^2$). The coalescence process starts at about $t = 0.5$ (second frame in the top row), where time is made dimensionless with respect to $a/U = \sqrt{\rho a^3/\sigma}$, and is already completed at time $t = 1.5$ (third frame in the top row). Around this instant a strong negative curvature is still present in the upper and lower parts of the newly formed, continuous interface. The distributed surface stress pushes the inner fluid to diverge in the y direction, leading to an overall ellipsoidal shape of the drop with major axis aligned with the y direction (first frame in the third row of panels in the figure). The large curvature in correspondence of the tips then induces a pressure force that stops the motion and starts an opposite oscillation. Maximum kinetic energy occurs at about half oscillation period. All along the process, the viscous stress keeps on dissipating the energy of the system, until the equilibrium steady state is reached with a circular, uniform drop.

The curves in figure 8(*b*,*d*) show the phase profile along the x-axis, on the symmetry line of the system. By the time instant of the fourth panel on the second row the topology change is substantially completed, with the phase profile nearly uniform inside the drop.

A similar experiment, now with $M^* \ll Cn^2$ ($M^* = 10^{-6}$) is reported in figure 9. The reconnection of the two initial droplets is apparent. However, a small island of zero phase forms in the middle of the drop and persists up to the steady state. On the basis of the theory of § 2.2 the phase profile is expected to be too stiff to promptly respond to the topology change. Since the expected inner/outer time scale ratio is $t/\tau = Cn^3/M^*$, we indeed conclude that the phase profile dynamics is too slow to adapt to the external time scale, over which the drop coalescence and the successive shape oscillation occur.

When the inner phase field is at equilibrium (tanh profile), the correct free energy of the system is basically given by the surface tension times the droplet surface area, at least near the sharp-interface limit. The equilibrium free energy is easily estimated beforehand, assuming a circular two-dimensional drop with the same two-

https://doi.org/10.1017/jfm.2012.461 Published online by Cambridge University Press

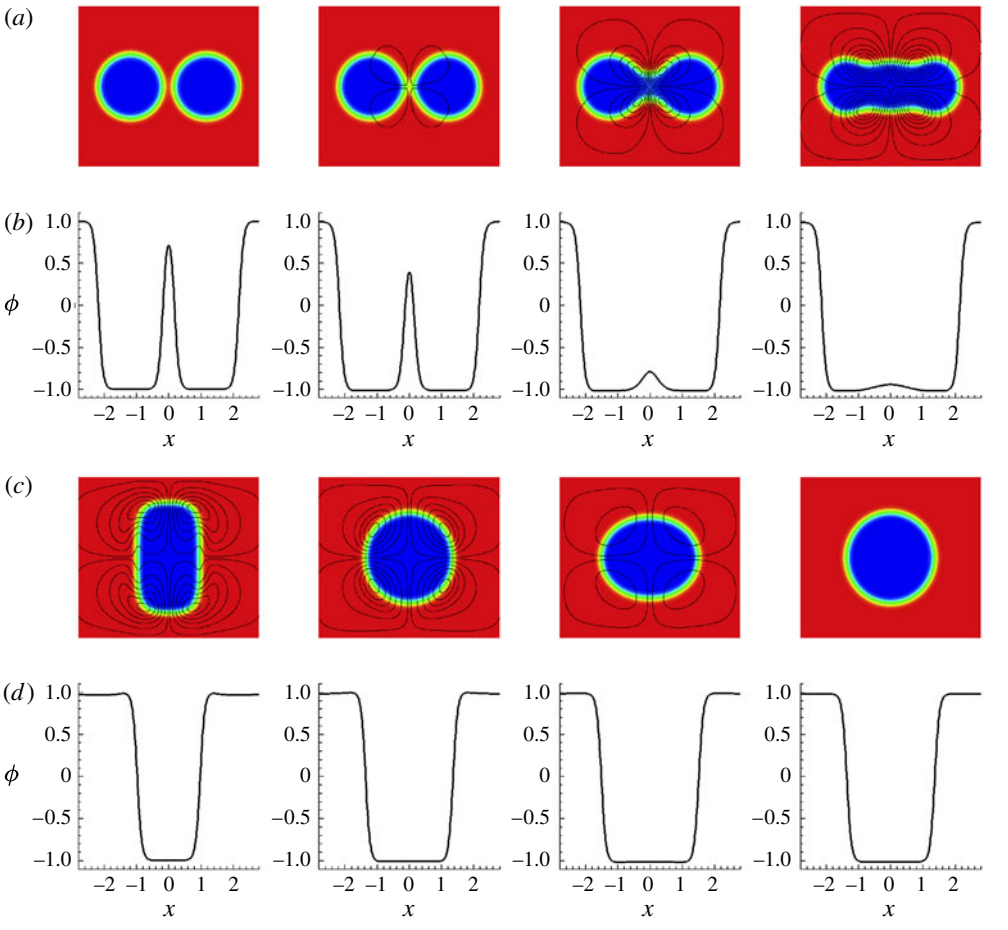


FIGURE 8. (Colour online) Drop coalescence dynamics with correct mobility. Snapshots of the phase field and flow streamlines (*a,c*, time increases from left to right and moving from top to bottom), and phase field profile versus x at $y = 0$ at corresponding time instants (*b,d*). Here $Cn = 0.1$ and $M^* = 0.01$. The configurations shown correspond to the time instants highlighted by the circles in figure 10.

dimensional volume of the two initial drops. Taking the initial radius a_i as the reference length scale, the dimensionless radius of the final drop then follows as $a_f^* = a_f/a_i = \sqrt{(2)}$, providing the sharp-interface limit of the equilibrium free energy as $F_{eq} = 2\pi a_f^*(2\sqrt{2}/3)$. The proportionality between free energy and surface of the drop allows us to directly link the time history of the free energy shown in figure 10 with the snapshots reported in figure 8. There, after coalescence, the drop takes on elongated configurations with interface area which oscillates in time between a lower bound provided by the final equilibrium shape and successive relative maxima which keep on decreasing until the equilibrium shape is reached. The solid line indicated by the arrow labelled F provides the free energy deprived of the estimated equilibrium free energy F_{eq} for $Cn = 0.05$ and mobility $M^* = Cn^2 = 2.5 \times 10^{-3}$. We see that the expected equilibrium free energy is indeed recovered once the steady-state solution is eventually achieved. Figure 10 also reports the kinetic energy of the fluid, solid line

https://doi.org/10.1017/jfm.2012.461 Published online by Cambridge University Press

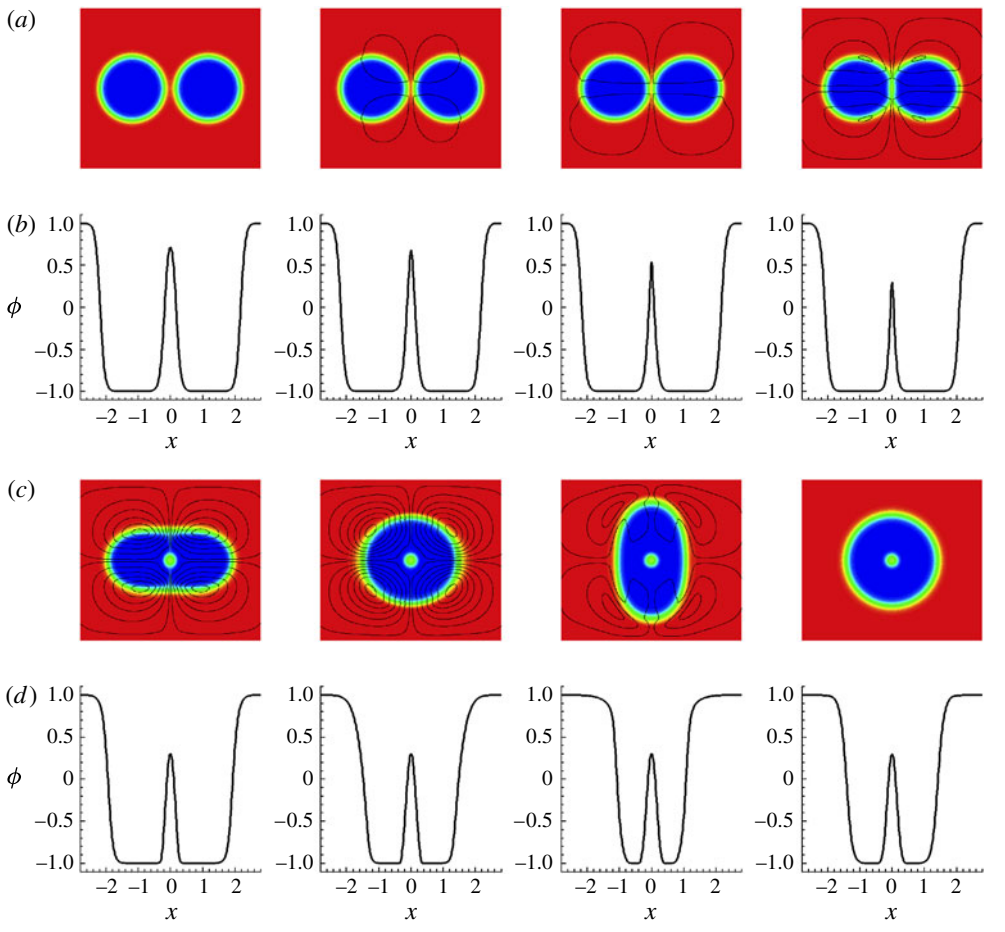


FIGURE 9. (Colour online) Incorrect drop coalescence dynamics induced by inappropriate mobility. Snapshots of the phase field and flow streamlines (*a,c*) and phase field profile versus x at $y = 0$ (*b,d*). Here $Cn = 0.1$ and $M^* = 10^{-6}$. Same time ordering as in figure 8.

marked by the arrow labelled K. The kinetic energy oscillates with opposite phase with respect to the free energy between zero and maxima which consistently decrease in time up to the point where the motion of the fluid stops. The two curves are enveloped by their sum, the total free energy F_T, which is a monotonically decreasing function of time. The dotted lines correspond to the same three quantities, now for a twice as large Cahn number, $Cn = 0.1$, with the same prescription for the mobility, $M^* \propto Cn^2$. The direct comparison between the results at $Cn = 0.1$ (dotted lines) and $Cn = 0.05$ (solid lines) shows that convergence of the results is indeed satisfactory. Quantitative data concerning convergence at reducing Cahn number using the optimal mobility are provided in table 2, where the error is estimated at the eventual steady state. As already discussed, it is easy to quantify the free energy of the steady state on the basis of the sharp-interface model, whose prediction we take as the exact solution. The data in the table actually show a convergent trend towards the analytical values, with a substantially linear decrease with Cahn number of the error on the free energy.

https://doi.org/10.1017/jfm.2012.461 Published online by Cambridge University Press

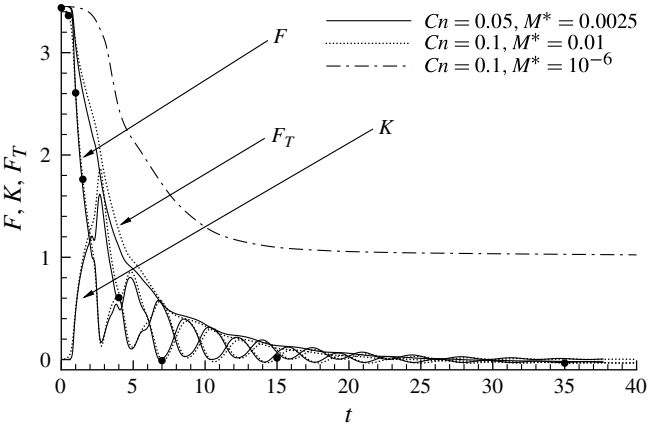


FIGURE 10. Time evolution of the free energy in the droplet coalescence problem. Solid and dotted lines denote data refinement by halving the Cahn number from $Cn = 0.1$ to $Cn = 0.05$, adapting the mobility according to the scaling law $M^* \propto Cn^2$ (see the legend). The equilibrium free energy F_{eq} estimated on the basis of the sharp-interface description has been subtracted from free energy curve (arrow labelled F). The kinetic energy (labelled K) oscillates out of phase and the total free energy F_T envelopes both curves. The closed circles denote the eight instants of time corresponding to the configurations reported in figure 8. The two sets of results show convergence to the correct dynamics with the free energy approaching the correct sharp-interface prediction. The dash-dotted line is the total free energy of a third case, with the same Cahn number as the solid line case and much smaller mobility (see the legend). The final, steady-state free energy is much larger than expected, suggesting a spurious metastable configuration.

Cn	Err (%)
0.1	3.5
0.05	2.4

TABLE 2. Error estimate at steady state for the drop coalescence problem: the diffuse-interface free energy is compared with the exact solution of the sharp-interface model, under the assumption that the steady state corresponds to a single circular drop of twice the volume of the two identical initial drops. When reducing the nominal interface thickness, $\propto Cn$, the mobility is reduced according to the prescription $M^* \propto Cn^2$.

The dash-dotted line of figure 10 provides the time history of the total free energy for a case with the same Cahn number of 0.1, now with a much smaller mobility $M^* = 1 \times 10^{-6}$, see figure 9. While in the first two cases $F - F_{eq}$ and $F_T - F_{eq}$ asymptote to zero for large times, in the small mobility case the inner profile is too stiff and unable to relax to form a single uniform drop, see the last image reported in figure 9. It is clear that the single, homogenous drop is still the equilibrium solution of minimal free energy, since at the steady state the mobility drops out from the equations. However, the system becomes unable to reach the equilibrium configuration and gets trapped in a metastable state spuriously formed due to the nearly frozen interface profile.

https://doi.org/10.1017/jfm.2012.461 Published online by Cambridge University Press

The results of the diffuse-interface model show that, under Cahn number refinement, the dynamics consists of a first phase where coalescence occur, leading to a single highly deformed drop. Successively a sequence of damped oscillations take place, where the energy stored in the deformed interface is released into kinetic energy, being meanwhile dissipated by viscosity. We conclude that refining the solution of the Cahn–Hilliard/Navier–Stokes model by reducing the interface thickness together with the mobility according to the rule suggested by the sharp-interface asymptotic limit provides the physically significant result also in the more complex case of topology changes.

4. Final comments and remarks

In this paper we have dealt with an open problem concerning the effectiveness of the Cahn–Hilliard/Navier–Stokes model in predicting the dynamics of unsteady binary flows of immiscible fluids. Apart from thermodynamic conditions near the critical point where the interface thickens, on the hydrodynamic scale the interface between the two fluids appears as a sharp discontinuity and its physical thickness emerges only at atomistic resolution. As a consequence a diffuse-interface approach has to be intended as a way to describe the evolution on mesoscopic spatial and temporal scales. The mesoscopic dynamics is indeed parameterized in terms of effective interface thickness and mobility which are not intrinsic physical properties. The open questions the paper contribute to answer concern: (i) the existence of a sharp-interface limit (i.e. the small thickness asymptotic state where the system evolution becomes independent of the effective parameters); (ii) how should it be achieved; (iii) the relationship between mobility and thickness; and (iv) the way correct physical properties of the interface are recovered.

Several authors established different criteria for selecting Cahn number and mobility, sometimes based on empirical demonstrations, other times attacking the problem on the side of asymptotic expansions. We reconsidered the issue on a firm theoretical basis, by a careful asymptotic analysis of the governing equations with no *a priori* preconception on the form the scaling parameter should have and leaving freedom to the theory to determine it as part of the solution process. The solution is split in inner and outer contributions and the diffuse interface is thoroughly discussed by analysing the inner expansion. The proper matching between inner and outer field unequivocally determines a scaling law for the mobility in terms of interface thickness. The ensuing scaling relationship, $M^* = \alpha Cn^2$, is shown to provide to correct recipe to balance the two antagonist driving mechanisms of outer and inner layer. On the one hand, a small mobility ($M^* \leqslant \beta Cn$) is needed in order to correctly describe the advection of the interface by the outer solution. On the other hand, the mobility should be sufficiently large ($M^* \geqslant \gamma Cn^3$) to keep the response time of the inner layer fast enough to provide the correct surface tension to the outer field. In addition to the two (inner and outer) spatial scales which emerge quite naturally in the problem, careful analysis of the dissipation processes revealed the existence of the fast time scale which drives the inner layer. The chemical free-energy dissipation associated with the phase field gradient inside the interface is indeed extremely fast. Mechanical equilibrium, coherently with the interaction with a smoothly evolving outer solution, is found to imply a Young–Laplace-like relation between curvature and pressure difference across the inner layer.

https://doi.org/10.1017/jfm.2012.461 Published online by Cambridge University Press

The theory has been applied to two specific problems, namely the propagation of capillary waves on the interface and the coalescence of two droplets. These two examples can be considered as reference cases for a large class of problems where the interfacial dynamics is crucial. The overall error in a specific simulation consists of two contributions: one associated with the convergence of the diffuse-interface model to the hydrodynamics (sharp-interface) description, the other associated with the convergence of the numerical scheme. Using well-accepted numerical algorithms, the main target was characterizing the model error as a function of the two effective parameters of the model. The numerical results confirm the theoretical scaling law between optimal mobility parameter and Cahn number and suggest the prefactor, leading to $M^*_{opt} \simeq 3Cn^2$. The same scaling law is numerically demonstrated to be able to provide the correct dynamics for the droplet coalescence problem.

We deem the present result extremely encouraging in view of the ever-increasing applications of the Cahn–Hilliard/Navier–Stokes model to more complex interfacial problems where the interface is thin and topology changes may occur in the system as a consequence of, e.g. droplet break-up, coalescence or highly nonlinear interface deformations. In these applications the elementary problems that have been addressed in the present paper are intrinsically combined, needing to bridge the two complementary dynamics occurring on the outer and the inner time scale. Typically one expects the topology change to take place after an elapsed, outer scale, time T. The inner layer dynamics evolves instead in the internal fast time $\tau = M^*/Cn^3 t$ and requires a time step scaling in inner variables, $\Delta\tau$, say. The prescription $M^* \propto Cn^2$ leads to $\Delta t = Cn\Delta\tau$, hence to a number of time steps needed to reach the coalescence time T given by $N = T/(Cn\Delta\tau)$. Clearly there is an unavoidable, but acceptable, cost in getting better and better convergence associated with the increase of required time steps and with finer and finer grid sizes.

Acknowledgements

This work was supported by the Standard HPC-2011 Grant (number std11-455) providing CPU time and storage at the CASPUR High Performance Computing Center.

Appendix

The outer profile actually shown in figure 3(*b*) is the zero-Cahn-number extrapolation $w_0^{(e)}$ of the data pertaining to three different simulations at progressively reduced Cahn number, Cn_s, $s = 1, \ldots, 3$ ($Cn_1 = 0.02$, $Cn_2 = 0.01$, $Cn_3 = 0.005$, $M^*_s = 3Cn_s^2$), according to the asymptotic expansion $w^{(e)}(\zeta, t; Cn) = w_0^{(e)}(\zeta, t) + Cn w_1^{(e)}(\zeta, t) + Cn^2 w_2^{(e)}(\zeta, t)$. The three terms of the expansion are obtained by solving the system

$$w_0^{(e)}(x, \zeta, t) + Cn_s w_1^{(e)}(x, \zeta, t) + Cn_s^2 w_2^{(e)}(x, \zeta, t) = w^{(e)}(x, \zeta, t; Cn_s), \quad s = 1, \ldots, 3, \tag{A 1}$$

at given t, x and ζ. The solid line superimposed to the extrapolated numerical data is the analytical solution provided in Prosperetti (1981), where the interface elevation of the standing wave at fixed $x = 1/2$ is explicitly described in terms of the function $a = a(t)$ as $z_I(x, t)|_{x=1/2} = \delta a(t)$. The displacement velocity of the interface

https://doi.org/10.1017/jfm.2012.461 Published online by Cambridge University Press

is then $w_I(x,t)|_{x=1/2} = \delta\dot{a}(t)$ which, given the interface condition $w(x,\zeta,t)|_{x=1/2,\zeta=0} = w_I(x,t)|_{x=1/2}$, fixes the analytical profile

$$w_a(\zeta,t) = \delta\dot{a}(t)\frac{\sinh\left[\dfrac{2\pi}{\lambda}(H/2-|\zeta|)\right]}{\sinh\left(\dfrac{2\pi}{\lambda}H/2\right)} \simeq \delta\dot{a}(t)\mathrm{e}^{-2\pi|\zeta|/\lambda}. \tag{A 2}$$

Here the deep-layer approximation in the rightmost side is in any respect indistinguishable from the exact solution for $H/(2\lambda) = 1$. A slight outward shift of the extrapolated zero-order term with respect to the analytical solution appears in figure 3(*b*). The shift is the effect of the displacement thickness associated with the constant velocity in the inner layer. It is expected to decrease by using data at smaller Cahn numbers.

REFERENCES

ARIS, R. 1989 *Vectors, Tensors, and the Basic Equations of Fluid Mechanics*. Dover.

BADALASSI, V. E., CENICEROS, H. D. & BANERJEE, S. 2003 Computation of multiphase systems with phase field models. *J. Comput. Phys.* **190** (2), 371–397.

CAHN, J. W. & HILLIARD, J. E. 1958 Free energy of a nonuniform system. I. Interface free energy. *J. Chem. Phys.* **28** (2), 258–267.

CAHN, J. W. & HILLIARD, J. E. 1959 Free energy of a nonuniform system. III. Nucleation in a two-component incompressible fluid. *J. Chem. Phys.* **31**, 688.

CARLSON, A., BELLANI, G. & AMBERG, G. 2012 Contact line dissipation in short-time dynamic wetting. *EPL (Europhys. Lett.)* **97**, 44004.

CARLSON, A., DO-QUANG, M. & AMBERG, G. 2009 Modeling of dynamic wetting far from equilibrium. *Phys. Fluids* **21**, 121701.

CHANDRASEKHAR, S. 1961 *Hydrodynamic and Hydromagnetic Stability*. Dover.

DING, H., GILANI, M. N. H. & SPELT, P. D. M. 2010 Sliding, pinch-off and detachment of a droplet on a wall in shear flow. *J. Fluid Mech.* **644** (217), 56.

FISK, S. & WIDOM, B. 1969 Structure and free energy of the interface between fluid phases in equilibrium near the critical point. *J. Chem. Phys.* **50**, 3219.

GIACOMELLO, A., MELONI, S., CHINAPPI, M. & CASCIOLA, C. M. 2012 Cassie–Baxter and Wenzel states on a nanostructured surface: phase diagram, metastabilities, and transition mechanism by atomistic free energy calculations. *Langmuir* **28**, 10764–10772.

GURTIN, M. E., POLIGNONE, D. & VINALS, J. 1995 Two-phase binary fluids and immiscible fluids described by an order parameter. *Math. Models Methods Appl. Sci.* **06**, 815, doi:10.1142/S0218202596000341.

HIRT, C. W. & NICHOLS, B. D. 1981 Volume of fluid (VOF) method for the dynamics of free boundaries* 1. *J. Comput. Phys.* **39** (1), 201–225.

HUANG, J. J., SHU, C. & CHEW, Y. T. 2009 Mobility-dependent bifurcations in capillarity-driven two-phase fluid systems by using a lattice Boltzmann phase-field model. *Intl J. Numer. Meth. Fluids* **60** (2), 203–225.

JACQMIN, D. 1999 Calculation of two-phase Navier–Stokes flows using phase-field modeling. *J. Comput. Phys.* **155** (1), 96–127.

JACQMIN, D. 2000 Contact-line dynamics of a diffuse fluid interface. *J. Fluid Mech.* **402**, 57–88.

JENG, U. *et al*. 1998 Viscosity effect on capillary waves at liquid interfaces. *J. Phys.: Condens. Matter* **10**, 4955.

KEVORKIAN, J. & COLE, J. D. 1996 *Multiple Scale and Singular Perturbation Methods,* vol. 114. Springer.

KHATAVKAR, V. V., ANDERSON, P. D. & MEIJER, H. E. H. 2006 On scaling of diffuse-interface models. *Chem. Engng Sci.* **61** (8), 2364–2378.

https://doi.org/10.1017/jfm.2012.461 Published online by Cambridge University Press

KIM, J. 2005 A continuous surface tension force formulation for diffuse-interface models. *J. Comput. Phys.* **204** (2), 784–804.

LIGHTHILL, J. 2001 *Waves in Rluids*. Cambridge University Press.

LOWENGRUB, J. & TRUSKINOVSKY, L. 1998 Quasi–incompressible Cahn–Hilliard fluids and topological transitions. *Proc. R. Soc. Lond. Ser.* A: *Math., Phys. Engng Sci.* **454**, 2617.

MARMOTTANT, P. & VILLERMAUX, E. *et al*. 2004 On spray formation. *J. Fluid Mech.* **498** (1), 73–111.

MENARD, T., TANGUY, S. & BERLEMONT, A. 2007 Coupling level set/VOF/ghost fluid methods: validation and application to 3D simulation of the primary break-up of a liquid jet. *Intl J. Multiphase Flow* **33** (5), 510–524.

MITRINOVIĆ, D. M., TIKHONOV, A. M., LI, M., HUANG, Z. & SCHLOSSMAN, M. L. 2000 Noncapillary-wave structure at the water–alkane interface. *Phys. Rev. Lett.* **85**, 582–585.

NIJMEIJER, M. J. P., BAKKER, A. F., BRUIN, C. & SIKKENK, J. H. 1988 A molecular dynamics simulation of the Lennard–Jones liquid–vapour interface. *J. Chem. Phys.* **89**, 3789.

ORLANDINI, S., MELONI, S. & CICCOTTI, G. 2011 Hydrodynamics from statistical mechanics: combined dynamical-NEMD and conditional sampling to relax an interface between two immiscible liquids. *Phys. Chem. Chem. Phys.* **13** (29), 13177–13181.

PROSPERETTI, A. 1981 Motion of two superposed viscous fluids. *Phys. Fluids* **24**, 1217.

QIAN, T., WANG, X. P. & SHENG, P. 2006 A variational approach to moving contact line hydrodynamics. *J. Fluid Mech.* **564**, 333–360.

REN, W. *et al*. 2011 Derivation of continuum models for the moving contact line problem based on thermodynamic principles. *Commun. Math. Sci.* **9** (2), 597–606.

RENARDY, Y. & RENARDY, M. 2002 Prost: a parabolic reconstruction of surface tension for the volume-of-fluid method. *J. Comput. Phys.* **183** (2), 400–421.

SEPPECHER, P. 1996 Moving contact lines in the Cahn–Hilliard theory. *Intl J. Engng Sci.* **34** (9), 977–992.

SUSSMAN, M. & PUCKETT, E. G. 2000 A coupled level set and volume-of-fluid method for computing 3d and axisymmetric incompressible two-phase flows. *J. Comput. Phys.* **162** (2), 301–337.

THORSEN, T., ROBERTS, R. W., ARNOLD, F. H. & QUAKE, S. R. 2001 Dynamic pattern formation in a vesicle-generating microfluidic device. *Phys. Rev. Lett.* **86** (18), 4163–4166.

TRIEZENBERG, D. G. & ZWANZIG, R. 1972 Fluctuation theory of surface tension. *Phys. Rev. Lett.* **28** (18), 1183–1185.

TRUESDELL, C. & TOUPIN, R. A. 1960 Principles of classical mechanics and field theory. In *Encyclopedia of Physics* (ed. S. Flügge). vol. 3. Springer, Part 1.

TRYGGVASON, G., BUNNER, B., ESMAEELI, A., JURIC, D., AL-RAWAHI, N., TAUBER, W., HAN, J., NAS, S. & JAN, Y. J. 2001 A front-tracking method for the computations of multiphase flow. *J. Comput. Phys.* **169** (2), 708–759.

UNVERDI, S. O. & TRYGGVASON, G. 1992 A front-tracking method for viscous, incompressible, multi-fluid flows. *J. Comput. Phys.* **100** (1), 25–37.

VOLLMAYR-LEE, B. P. & RUTENBERG, A. D. 2003 Fast and accurate coarsening simulation with an unconditionally stable time step. *Phys. Rev.* E **68** (6), 66703.

VAN DER WAALS, JD 1979 The thermodynamic theory of capillarity under the hypothesis of a continuous variation of density. *J. Stat. Phys.* **20** (2), 200–244.

YUE, P., FENG, J. J., LIU, C. & SHEN, J. 2004 A diffuse-interface method for simulating two-phase flows of complex fluids. *J. Fluid Mech.* **515**, 293–317.

YUE, P., FENG, J. J., LIU, C. & SHEN, J. 2005 Diffuse-interface simulations of drop coalescence and retraction in viscoelastic fluids. *J. Non-Newtonian Fluid Mech.* **129** (3), 163–176.

YUE, P., ZHOU, C. & FENG, J. J. 2010 Sharp-interface limit of the Cahn–Hilliard model for moving contact lines. *J. Fluid Mech.* **645**, 279–294.

https://doi.org/10.1017/jfm.2012.461 Published online by Cambridge University Press